

AJL 2145

THEORY AND APPLICATIONS OF Si/Si_{1-x}Ge_x SUPERLATTICES ON
VOLTAGE TUNABLE INFRARED DETECTORS

By

SUNGMIN CHO

A DISSERTATION PRESENTED TO THE GRADUATE SCHOOL
OF THE UNIVERSITY OF FLORIDA IN PARTIAL FULFILLMENT
OF THE REQUIREMENTS FOR THE DEGREE OF
DOCTOR OF PHILOSOPHY

UNIVERSITY OF FLORIDA

1992

ACKNOWLEDGEMENTS

The author wishes to express his sincere gratitude toward Dr. Hong H. Lee, chairman of the advisory committee, for his patience and continued guidance throughout this work. Thanks are also due to Dr. S. A. Svoronos, Dr. T. J. Anderson, Dr. M. E. Orazem, Dr. C.-W. Park, and Dr. P. S. Zory for their time on the advisory committee. Special thanks are extended to Dr. S. A. Svoronos for serving as a cochairman of the committee.

The author also wishes to express his gratitude to his colleagues J. S. Yoo, J. V. Cole, D. C. Koopman, C. H. Park, and H. D. Lee for their valuable comments and suggestions.

Sincere appreciation is extended to his parents, brothers, sister, wife and child for their support and encouragement which made this work possible.

TABLE OF CONTENTS

	Page
ACKNOWLEDGEMENTS	ii
ABSTRACT	v
CHAPTERS	
1 INTRODUCTION	1
2 CONDUCTION ENERGY BAND STRUCTURE OF Si/Si _{1-x} Ge _x SUPERLATTICES	8
Introduction	8
Description of the Method	10
Applications and Results	19
Conclusion	26
3 INTERSUBBAND OPTICAL ABSORPTION IN Si/Si _{1-x} Ge _x SUPERLATTICE	30
Introduction	30
Conduction Band Structure	31
Intersubband Absorption Coefficient	35
Summary	41
4 ELECTRIC FIELD EFFECT ON INTERSUBBAND OPTICAL ABSORPTION IN Si/Si _{1-x} Ge _x SUPERLATTICE	43
Introduction	43
Theory	45
Intersubband Optical Transition	53
Conclusion	61
5 IMPACT IONIZATION COEFFICIENT AND ENERGY DISTRIBUTION FUNCTION IN POLAR AND NONPOLAR SEMICONDUCTOR	63
Introduction	63

The Boltzmann Transport Equation	65
Impact Ionization Coefficients	69
Comparison and Discussion	78
Conclusion	91
 6 VOLTAGE TUNABLE INFRARED DETECTORS	92
Introduction	92
Band Aligned Superlattice	94
Stepped Well Superlattice	100
Concluding Remarks	102
 APPENDICES	
A THE $k \cdot p$ HAMILTONIAN FOR Ge AND Si IN THE [100] DIRECTION	105
B ELEMENTS OF THE TRANSFER MATRIX FOR BULK, <u>M</u>	112
C CONDUCTIVITY EFFECTIVE MASS	113
REFERENCES	115
BIOGRAPHICAL SKETCH	121

Abstract of Dissertation Presented to the Graduate School
of the University of Florida in Partial Fulfillment of the
Requirements for the Degree of Doctor of Philosophy

**THEORY AND APPLICATIONS OF Si/Si_{1-x}Ge_x SUPERLATTICES ON
VOLTAGE TUNABLE INFRARED DETECTORS**

By

SUNGMIN CHO

December, 1992

Chairman : Hong H. Lee

Major Department : Chemical Engineering

Theoretical studies on Si/Si_{1-x}Ge_x superlattices are carried out for an application to voltage tunable infrared detectors. First, the conduction band structures are presented for the superlattices using the transfer matrix method, and variation of miniband energies and the bandwidths is given as a function of the energy well or barrier width.

Subsequently, the absorption coefficient for intersubband transitions between the minibands in the superlattice is calculated using multicomponent envelope functions. The results are compared with those obtained by a single wave function approximation. Large differences in the absorption coefficient are found between the two cases. The differences are analyzed in terms of the charge densities of the wave functions and the momentum matrix elements for the intersubband transitions involved. It is found that the absorption coefficient estimate is much lower and most of the transition peaks are absent when the single wave function approximation is used.

The electric field effect on the intersubband optical absorption in the superlattice is also reported. Full spectra of the absorption coefficient are calculated from zero to high

electric fields. The effect of Wannier-Stark localization on intersubband transitions is theoretically studied for the superlattice and the charge densities are given for various electric fields. A finite length superlattice instead of an infinite superlattice is considered to show the effects of electric fields on the optical absorption. The Stark shift toward the shorter wavelength is observed.

An expression for the electron energy distribution function is derived using an approximate solution of the Boltzmann transport equation. In the derivation, all major scattering mechanisms are included, and a distinction is made between nonpolar and polar optical phonon scattering. Numerically calculated impact ionization coefficients for electrons and holes in Si, Ge, and GaAs compare favorably with almost all experimental results reported in the literature.

Finally, several Si/Si_{1-x}Ge_x superlattice structures are presented for an application to voltage tunable infrared detectors. The structures use concepts of band aligned superlattice and stepped well superlattices. In the structures, the voltage tunable detection could be realized by adjusting subband energy levels with an applied electric field.

CHAPTER 1 INTRODUCTION

Silicon and Germanium have been extremely important materials in the field of semiconductor electronics for the past few decades. Traditionally Si has been the material of choice for semiconductor electronics not only because of its electronic properties, but also because of its superior mechanical properties and the excellent insulating qualities of its oxide.¹ It is well known that the III-V compound semiconductors such as GaAs and InP, which have direct band gaps, have been applied for optoelectronic devices. Due to their indirect band gaps, however, Si and Ge have not been suitable for optoelectronics applications. As an example, the optical absorption strengths of pure Si and Ge are about 6 orders of magnitude lower than those of typical optoelectronic materials such as GaAs. However, recent advances in crystal growth techniques such as molecular-beam epitaxy (MBE) have allowed the fabrication of thin-layered epitaxial structures known as quantum heterostructures of quantum wells and superlattices,² which might significantly change the electrical and optical properties of the constituent materials. In particular, Si/Si_{1-x}Ge_x superlattices seem to offer the intriguing possibility of greatly enhancing the optical properties over pure Si and Ge. Since such structures can be easily integrated with highly advanced silicon processing technology, the study of Si/Si_{1-x}Ge_x superlattices is more attractive.

A semiconductor superlattice is formed from a series of alternating semiconductor materials with periodicity. The superlattice was first introduced by Esaki and Tsu² in 1970. Because of its periodically-layered structure, a superlattice can have an unique energy band structure and so could be considered as a new semiconductor crystal with an extended unit cell along the growth direction. It has the consequence of reducing the Brillouin zone in the growth direction and qualitatively folding the bulk energy band into the reduced zone. As a result of zone folding in the superlattice band structure, tailoring the superlattice energy band structure becomes possible. In that a superlattice can be engineered to have a certain electronic or optical property, the process used to be called band structure engineering.

Initially, superlattices were grown with III-V semiconductor compounds of GaAs and $\text{Al}_x\text{Ga}_{1-x}\text{As}$ because these two materials have almost perfectly matched lattice constants and so defect-free layers could be easily attained. The large lattice mismatch (about 4%) between Si and Ge, however, hampers the formation of dislocation-free interfaces. But using MBE, it has recently become possible to grow epitaxial layers without misfit defects between materials which are lattice mismatched by several percent. The first energy band calculations of silicon-based superlattices were published in 1975 (Ref.3) using an extended Kronig-Penney model, although the validity of the model has proven to be very limited. Since 1987, a series of publications on the energy band structures of $\text{Si}/\text{Si}_{1-x}\text{Ge}_x$ superlattices has appeared in which the band structures were calculated using the envelope function approximation (EFA)⁴⁻⁶ or the empirical pseudopotential method^{7,8}, while including strain effects. A limited number of studies is

reported to show the possibility of the applications of the superlattices for optoelectronic devices.^{9,10}

$\text{Si/Si}_{1-x}\text{Ge}_x$ heterostructures offer some interesting applications for electronic or optoelectronic solid-state devices. Some applications are described in the following. First, the structures show promise of having large optical matrix elements for intersubband transitions for normal incidence of light because of their anisotropic effective masses.¹¹⁻¹³ It should be a significant advantage over the conventional III-V semiconductor structures in which the matrix element for absorption of waves incident normal to the interface is zero and therefore gratings could be incorporated to increase the coupling efficiency of normal illumination. Secondly, the structures could be applied to resonant tunnelling devices.¹⁴ Since strain effects in the structures could induce splittings of the sixfold conduction bands into twofold and fourfold states and change the band-edge profiles considerably, the resonant tunnelling due to twofold, fourfold, or twofold and fourfold electrons can be selectively achieved by a proper choice of the layer thicknesses and alloy concentrations in the barrier layers. Using these phenomena it would be possible to make an electron filter and to realize many novel and interesting semiconductor devices through the integration of such structures with existing Si devices. Thirdly, a modulation doped $\text{Si/Si}_{1-x}\text{Ge}_x$ structure is known to have extremely high electron mobility.^{15,16} In addition to the high mobility, low sheet resistance and the proximity of the two-dimensional electron gas to the surface have been observed and indicate that such layers can be exploited for high transconductance modulation-doped field-effect transistors. Finally, a novel avalanche infrared photodetector is possible by using the $\text{Si/Si}_{1-x}\text{Ge}_x$ superlattices for

optical fiber communications. Due to the effect of bandgap narrowing by the strain in alloy layers, the fundamental absorption threshold of the superlattice is shifted to longer wavelengths, so that the detector can be operated in the range of silica-fiber transparency, 1.3–1.55 μm .^{17,18} In addition to the aforementioned possibilities, it has been recently predicted that optical transitions between conduction subbands of the superlattice could have large oscillator strengths, so that it could be exploited for infrared detectors.^{9,10} In this dissertation the intersubband infrared absorption in the Si/Si_{1-x}Ge_x superlattices is investigated and the electric field effect is examined.

Intersubband infrared absorption in multiple quantum wells has been extensively investigated because of its potential application to infrared detectors. For commercial infrared detectors, the HgCdTe, InSb, PbSe, and PbS detectors have been popular. In late 1980, the GaAs/Al_xGa_{1-x}As quantum well infrared detectors¹⁹⁻²² (QWIP) were first successfully demonstrated to exhibit high responsivity and detectivity, comparable to typical background-limited²³ HgCdTe photoconductive detectors. GaAs multiple quantum well detectors have been reported^{21,22} to have a number of potential advantages with respect to HgCdTe devices: GaAs growth, processing, and passivation technologies are more mature than those of HgCdTe; monolithic integration of these detectors with GaAs field-effect transistors (FET's), charge coupled devices (CCD's), and high-speed signal processing electronics should be possible; GaAs substrates are larger, cheaper, and of higher quality than CdTe substrates; GaAs MBE affords excellent uniformity, reproducibility, and composition control over 3 inch wafers; GaAs is more thermally stable than HgCdTe. In addition, due to an ease of varying the GaAs quantum well dimensions

as well as the composition and thickness of the $\text{Al}_x\text{Ga}_{1-x}\text{As}$ barriers, one can readily vary the peak absorption wavelength over the atmospheric window region $\lambda=8\text{--}14 \mu\text{m}$. With all those advantages, large-area focal plane arrays and high-speed detectors should be possible. However, since most of the readout devices are made of silicon for sensor-array type applications, silicon-based infrared detectors are of greater interest. Even though the question of band offsets has not been completely understood and the magnitude of the offsets are not certain, observations of two-dimensional electron gas revealed at least one case of type II alignment of bands with the $\text{Si}/\text{Si}_{1-x}\text{Ge}_x$ conduction band edge lying higher in energy than that in Si layers.²⁴ In principle, the complete infrared detection process of the multiple $\text{GaAs}/\text{Al}_x\text{Ga}_{1-x}\text{As}$ quantum wells can be followed in $\text{Si}/\text{Si}_{1-x}\text{Ge}_x$ quantum wells as well. Therefore, it is of interest to know whether the Si-based quantum wells can be utilized in infrared light detection if the necessary band offset can be achieved. Thanks to the progress of Si MBE, a few successful observations of intersubband absorption in $\text{Si}/\text{Si}_{1-x}\text{Ge}_x$ MQWs²⁵⁻²⁸ have recently been reported. Theoretically, Rajakarunanayake and McGill¹¹ calculated the absorption strengths for the intersubband transitions in *n*-type $\text{Si}/\text{Si}_{1-x}\text{Ge}_x$ superlattices, and peak absorption strengths of about $2000\text{--}6000 \text{ cm}^{-1}$ were obtained which are comparable to those in $\text{GaAs}/\text{Al}_x\text{Ga}_{1-x}\text{As}$ superlattice detectors. Similar results are also available elsewhere.^{12,13,29}

One of the properties which is important for many applications of intersubband quantum well detectors is a wide spectral response, preferably over the atmospheric window range $8\text{--}12 \mu\text{m}$ and tunability of the peak wavelength.^{30,31} It has been shown in a single or multiple quantum well that voltage tunable infrared detection can be realized by

adjusting the energy levels of subbands with an applied electric field.³¹⁻³³ It has the consequence of quantum-confined Stark shift under bias. While square quantum wells do not exhibit much intersubband shift under bias, a stepped quantum well infrared detector is known to greatly enhance the tunability, due to two different barrier widths. However, the voltage tunability might also be attained in a superlattice or band aligned (multistack) superlattice (BAS) structure in different ways and it will be treated in chapter 6 for the Si/Si_{1-x}Ge_x superlattices.

On the other hand, avalanche multiplication by impact ionization is another important process in semiconductor devices, in particular in avalanche photodetector and devices operating under high electric field. For low noise avalanche photodiode (APD), a large difference in the ionization rates for electrons and holes is known to be essential. Silicon has an ionization rate ratio $k = \alpha/\beta = 20$ and therefore is an ideal APD³⁴. Unfortunately, most III-V semiconductors which are currently used for optical devices have α nearly equal to β so that it is not suitable for an APD. This superiority of silicon over III-V semiconductors might be exploited in many applications for optoelectronic solid-state devices which would be possible in the near future.

The main objective of this dissertation is to investigate the possibility of using the Si/Si_{1-x}Ge_x superlattices for voltage tunable infrared detection. In order to achieve this goal the first four chapters are devoted to expanding our knowledge of quantum physics, especially with respect to Si/Si_{1-x}Ge_x superlattices. In chapter 2, the conduction band structures are calculated by using the EFA and the bandwidths are shown with variations of the width of energy well or barrier. The absorption coefficients for intersubband

infrared transitions are obtained in chapter 3 more rigorously with the multicomponent envelope functions than those reported previously with an approximation of single wave function, which have been only available so far. In chapter 4, the electric field effect on the optical properties of Si/Si_{1-x}Ge_x superlattices is examined to show the Wannier-Stark ladder formation and Stark shift under bias. In chapter 5, analytical forms for the impact ionization coefficients are given. The analytical derivation includes all the major scatterings occurred in polar and non-polar semiconductor materials and impact ionization scattering at high electric fields. The theory, however, is limited to bulk semiconductor materials at the present time unless the superlattices are considered to have average bulk properties. For an application of the Si/Si_{1-x}Ge_x superlattices for the voltage tunable infrared detector, two device structures are given in chapter 6. The suggested structures utilize ideas of the band aligned superlattice (BAS) and of resonant tunneling.

CHAPTER 2

CONDUCTION ENERGY BAND STRUCTURE OF Si/Si_{1-x}Ge_x SUPERLATTICES

2.1 Introduction

The original paper on semiconductor superlattices by Esaki and Tsu² generated widespread interest in the electrical and optical properties of these novel solid-state structures. The superlattices formed from alternating layers of GaAs and Al_xGa_{1-x}As have attracted the greatest attention since those layers have almost perfectly matched lattice constants, but it is well known that the superlattices can be fabricated from other III-V materials, II-VI materials , and silicon and germanium as well. The large lattice mismatch (~4%) between silicon and germanium obstructs the formation of dislocation-free interfaces, but recent developments on Si MBE made good quality Si and Si_{1-x}Ge_x interfaces possible.³⁵

Considerable effort has been given to calculate energy band structures of superlattice structures. The first of these works was published in 1975 (Ref. 3), and is in fact an extension of Kronig-Penney model. From experimental evidences provided from GaAs/Al_xGa_{1-x}As structures, the validity of this model is proven to be very limited. Subsequently, a series of publications has appeared in which the band structure is calculated using an empirical tight-binding method.^{36,37} This is considered to be the most reliable method for GaAs/Al_xGa_{1-x}As structures, but requires rather long computation time.

The envelope function approximation (EFA) is yet another method that has been developed for GaAs-based superlattices.^{4-6,38,39} In this method, the band structure of the bulk materials is described using the $\mathbf{k}\cdot\mathbf{p}$ method and the bands of the superlattice are then obtained by applying the effective mass approximation (EMA).⁴⁰ Since both GaAs and $\text{Al}_x\text{Ga}_{1-x}\text{As}$ have a direct band gap in the middle of the Brillouin zone, a correct description of the band structure of just the region around the Γ point suffices to obtain the bands of the associated superlattice. In this case, therefore, the Kane formalism is used, and a rather simple dispersion relation can be derived which is similar in shape to the results of a straightforward Kronig-Penney calculation. By comparing the results using the EFA to results based on the tight-binding calculation, it has been shown that the EFA has a wide range of validity.

In this chapter the application of the EFA to $\text{Si}/\text{Si}_{1-x}\text{Ge}_x$ superlattices is described. Crystal momentum in the transverse directions to the superlattice axis will be neglected. The calculation in this chapter could be considered as an extension of the III-V band structure calculation in the sense that a description of the bands valid across the entire Brillouin zone is used. This is necessary in order to take the equivalent conduction band minima in bulk silicon properly into account. The full Brillouin zone description makes the calculations more complicated, but it gives a more reliable energy band structure for multivalley semiconductor materials such as Si and $\text{Si}_{1-x}\text{Ge}_x$, which will be treated here.

2.2 Description of the Method

The effective mass approximation starts out with a description of the bands of the two constituent materials in the relevant part of the Brillouin zone using the $\mathbf{k}\cdot\mathbf{p}$ method. In this method, the energy of the bands at a certain value of the crystal momentum k is given by the solution of an algebraic eigenvalue equation. For the [100] direction being considered, the Δ_1 bands, to which the lowest conduction band in silicon belongs, are given by Cardona and Pollak⁴¹ as the eigenvalues of the matrix

$$\begin{bmatrix} E_{15} + k_x^2 & Tk_x & T'k_x \\ Tk_x & E_1'' + k_x^2 & 0 \\ T'k_x & 0 & E_1' + k_x^2 \end{bmatrix}. \quad (2.1)$$

Here, E_{15} , E_1' , and E_1'' are the zone-center energies corresponding to the Γ_{15} , Γ_1' , and Γ_1'' states, respectively, comprising the Δ_1 bands, and T and T' are the momentum parameters indicating the level of interactions between Γ_{15} and Γ_1'' states for T and Γ_{15} and Γ_1' states for T' . The derivation of the above Hamiltonian matrix of Δ_1 bands is briefly described in Appendix A. For an energy level, the characteristic equation is cubic in k^2 , yielding six roots in pairs of \mathbf{k} and $-\mathbf{k}$, two of which are physically meaningless.

In the study of the conduction band for a Si/Si_{1-x}Ge_x superlattice, de Sterke and Hall⁴ dropped the k_x^2 term associated with E_1' in Eq.(2.1) for mathematical convenience. Although the practice yields approximate results, it is nevertheless physically unacceptable in that the first-order (perturbation) correction term to the empty lattice to represent the filled lattice is completely neglected, defeating the very purpose of $\mathbf{k}\cdot\mathbf{p}$ correction for the

outlying Γ_1^l state. Lee,⁶ on the other hand, calculated the band structure with the full matrix as given by Eq.(2.1), retaining the k_x^2 in the (3,3) element. Applying the EMA, and turning \mathbf{k} into $-i\nabla$, the following set of differential equations results,

$$\begin{aligned} \left[E_{1s} - \frac{d^2}{dx^2} \right] F_1 - iT \frac{d}{dx} F_2 - iT' \frac{d}{dx} F_3 &= EF_1, \\ -iT \frac{d}{dx} F_1 + \left[E_1^u - \frac{d^2}{dx^2} \right] F_2 &= EF_2, \\ -iT' \frac{d}{dx} F_1 + \left[E_1^l - \frac{d^2}{dx^2} \right] F_3 &= EF_3. \end{aligned} \quad (2.2)$$

The differential equation for the envelope functions for the full matrix can be satisfied by the following solutions:

$$\begin{aligned} F_1 &= -A\lambda_1 \sin(k_1 x) + B\lambda_1 \cos(k_1 x) - C\lambda_2 \sin(k_2 x) + D\lambda_2 \cos(k_2 x), \\ F_2 &= B\sin(k_1 x) + A\cos(k_1 x) + D\sin(k_2 x) + C\cos(k_2 x), \\ F_3 &= \frac{B\lambda_1}{\alpha_1} \sin(k_1 x) + \frac{A\lambda_1}{\alpha_1} \cos(k_1 x) + \frac{D\lambda_2}{\alpha_2} \sin(k_2 x) + \frac{C\lambda_2}{\alpha_2} \cos(k_2 x), \end{aligned} \quad (2.3)$$

where k_1 and k_2 are the wave vectors resulting from the characteristic equations, F_i 's are the envelope functions, and λ_i 's and α_i 's are given by

$$\begin{aligned}\lambda_i &= \frac{E - E_1^u - k_i^2}{iT k_i}, \quad i = 1, 2; \\ \alpha_i &= \frac{E - E_1^l - k_i^2}{iT' k_i}, \quad i = 1, 2.\end{aligned}\tag{2.4}$$

Of the three roots obtainable from Eq.(2.1), only those within the Brillouin zone are used, which are k_1 and k_2 . The fact that only two wave vectors are sufficient to satisfy the three envelope functions means that any one of the three is a linear function of the other two. This fact can be used to write the following differential equations from Eq.(2.1):

$$\frac{d}{dx} \left[\left(-1 + T^2 / \gamma \right) \frac{dF_1}{dx} \right] - \left(iT - iT' \beta / T \gamma \right) \frac{dF_2}{dx} = (E - E_{15}) F_1,$$

and (2.5)

$$-\frac{d^2 F_2}{dx^2} - iT \frac{dF_1}{dx} = (E - E_1^u) F_2,$$

where

$$\gamma = \frac{(E - E_1^l - k_1^2)(E - E_1^l - k_2^2)}{E_1^l - E_1^u},$$

$$\beta = \frac{(E - E_1^u - k_1^2)(E - E_1^u - k_2^2)}{E_1^u - E_1^l}.$$

The connection rules are that F_1 and F_2 are continuous and that $(-1+T'^2/\gamma)dF_1/dx$ and dF_2/dx are also continuous over an interface.

For consistency, the momentum matrix elements T and T' in Eq. (2.1) should be the same for the two constituent materials of the superlattice. Although the values for one constituent material have been used for the other in direct-band-gap semiconductors as in GaAs/Al_xGa_{1-x}As in the past,³⁹ average values of T and T' for Si and Ge are used as in Lee's work.⁶ This necessitates adjustment of the energy levels of the zone-center states so as to represent properly the lowest Δ_1 band in both Si and Ge. In Lee's work,⁶ values of E_1^l and E_1^u are adjusted with the constraints that the band minimum is the same and the difference between his values and those calculable from the parameters by Cardona and Pollak is minimized. The value of E_{15} is left unchanged so that the zone-center value for the lowest Δ_1 band remains the same. The parameter values thus determined are given in Table 2.1.⁶ In the energy range of interest, the lowest Δ_1 band calculated with the values in Table 2.1 is within 2% of those calculated with the values given by Cardona and Pollak.⁴¹ The method described so far is applied to the Si/Si_{1-x}Ge_x

Table 2.1. Parameter values used for band structure of bulk materials in atomic units. The origin of energy is at the valence-band maximum.

Parameter	Si	Ge
E_{15}	0.252	0.232
E_1^u	0.566	0.536
E_1^l	-1.2196	-0.7055
T	1.14	1.14
T'	0.369	0.369

superlattices mostly with $x=0.5$, the superlattice for which the band offset is well established. The band offset of 0.3 eV is used with Si as the well material for the case.

The superlattice band structure can be obtained by imposing the Bloch condition which requires that

$$F(x + d) = e^{iqd} F(x) \quad (2.6)$$

where F is the column matrix with elements

$$(F_1(x), F_2(x), F_1'(x), F_2'(x))^T, \quad (2.7)$$

d is the period of the superlattice (SL), and q is the superlattice wave vector that signifies the crystal momentum in the SL. The connection rules stated above can be written in the form of a diagonal matrix that operates on the vector with components given in Eq. (2.7);

$$\begin{bmatrix} 1 & 0 & 0 & 0 \\ 0 & 1 & 0 & 0 \\ 0 & 0 & \frac{1-T'^2(E_1^{l,A}-E_1^{u,A})/(E-E_1^{l,A}-k_{1,A}^2)(E-E_1^{l,A}-k_{2,A}^2)}{1-T'^2(E_1^{l,B}-E_1^{u,B})/(E-E_1^{l,B}-k_{1,B}^2)(E-E_1^{l,B}-k_{2,B}^2)} & 0 \\ 0 & 0 & 0 & 1 \end{bmatrix} \quad (2.8)$$

(for transfer from material A to material B). This transfer matrix for an interface, together with the matrix for transfer through the materials given in Appendix B, allow us to determine the envelope functions anywhere in the structure. To propagate the

envelope functions over one period of the SL, the two types of transfer matrices have to be multiplied in the appropriate order.

The Bloch condition of Eq. (2.6) means that one has to determine the eigenvalues of the overall transfer matrix over a single period. A proper way to find the eigenvalues can be devised by realizing that since the positive and negative x directions are fully equivalent; given that $\exp(iqd)$ is an eigenvalue, $\exp(-iqd)$ must be an eigenvalue as well. Hence, The four eigenvalues of the overall transfer matrix can be written as $\exp(iq_1d)$, $\exp(-iq_1d)$, $\exp(iq_2d)$, $\exp(-iq_2d)$. The trace of the matrix is the sum of the eigenvalues, or $2\cos(q_1d)+2\cos(q_2d)$. The product of the two cosine terms can be found in a similar way.

$$\cos(q_1d) + \cos(q_2d) = \frac{1}{2}(M_{tr}), \quad (2.9)$$

$$\cos(q_1d)\cos(q_2d) = \frac{1}{4} \left(-2 + \sum_{j>i} M_{ii}M_{jj} - \sum_{j>i} M_{ij}M_{ji} \right),$$

where q_1 and q_2 are the wave vectors, M_{tr} is the trace of the overall transfer matrix, and M_{ij} are the elements of the matrix. The solution of these two equations is made easier by the fact that the right hand side of both equations are real. The expressions for the elements cannot be given analytically but the values could be obtained from proper multiplications of the transfer matrices for both interfaces (Eq.(2.8)) and bulk (Appendix B). The two wave vectors can lead to a doublet for the superlattice bands.

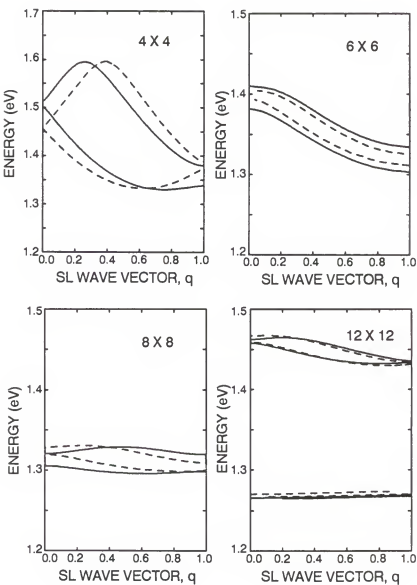


Fig.2.1. Band structures for $\text{Si}/\text{Si}_{1-x}\text{Ge}_x$ superlattices. The solid lines represent the present results and the dashed lines are obtained by a single wave function approximation.

The results are shown for four different structures of the superlattices in Fig.2.1. The solid curves represent the present results while the dashed ones the results of de Sterke and Hall.⁴ The Fig.2.1 implies that the exclusion of the (3,3) element in Eq. (2.1) can result in slight changes from the band structures which are obtained with the full 3×3 Hamiltonian of Eq. (2.1) even though the general trend is kept the same. The band structure which is calculated by the empirical pseudopotentials supports that the band structure obtained with the inclusion of (3,3) element is more accurate than that without the element. While a quantum well structure has flat energy bound states, the superlattice energy bands are dispersed in energy over the superlattice wave vector, due to interactions between bound states in adjacent wells. Since the interactions becomes stronger with a relatively narrower barrier to a well, the bandwidth becomes wider in energy as the width of barrier decreases. The miniband, which refers to the dispersed energy band in a superlattice, is very important for the study of carrier transport in the growth direction. When a band aligned superlattice is considered, the bandwidth of the miniband is necessarily known for accomplishing the band alignment.

While the real crystal potential has the same period as the lattice points, the period of the superlattice potential is the same as the alternating layers. For convenience, one period of the alternating layers will be called the basis of the superlattice. In the bulk semiconductor, different bases or primitive cells will result in different crystal potentials, thus different energy bands. Analogously, one may expect that the minibands in the superlattice will change as the superlattice basis changes. In the past since its inception in 1970 (Ref.2), the imposed superlattice basis has mostly been simple single well and barrier

structure for simplicity of analysis. With modification of the basis, interesting effects are expected in the miniband transport and optical transitions. In the following section, variable basis superlattices, which include square well, stepped well, and two-well coupling superlattices, are studied. The bandwidth variation is also given with respect to the variable width of the well or barrier.

2.3 Applications and Results

A. Square well superlattice

The miniband energies versus well or barrier width (number of monolayers) are shown in Figs. 2.2-2.4. The bandwidth, which is shown as the dotted area in the figures, accounts for energy spacing between the lowest and highest energy of a certain band. If the two doublets are overlapped in energy, only a bandwidth of the doublets could appear. Otherwise, the bandwidth could be divided by two energy ranges, corresponding to the two doublets. The islands which lie inside the dotted bandwidth area in the figures represent the case when the doublets are separated in energy. The bandwidth variation of the superlattice with equal widths of well and barrier is shown in Fig.2.2. The crisscross behavior of the energy levels is due to the intervalley mixing effect. This is one of the unique electronic properties of multivalley semiconductors. Due to the multivalley nature, each electronic state of this material can be represented as linear combinations of two states whose Fourier transforms in wave vector space are located in the two equivalent valleys. The scattering of electrons from the interfacial boundaries leads to the intervalley mixing. This mixing could be substantial due to the abruptness of the interface

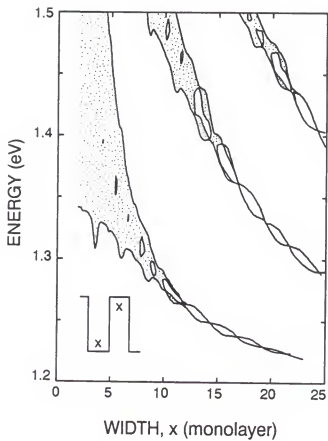


Fig. 2.2. The miniband energies versus equal well and barrier width.

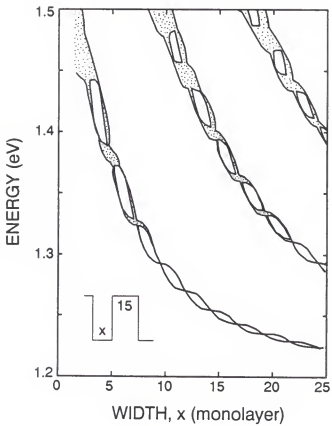


Fig. 2.3. The miniband energy versus well width. The barrier width is fixed to 15 monolayers.

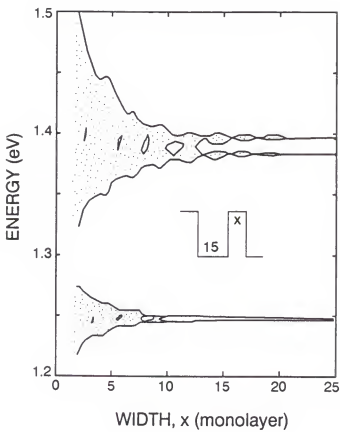


Fig. 2.4. The miniband energies versus barrier width. The well width is fixed to 15 monolayers.

potential. In the absence of intervalley mixing, the energy spectrum would be similar to a single-valley superlattice, except that each energy level would be doubly degenerate, corresponding to the states derived from the two equivalent valleys. Intervalley mixing splits this degeneracy and leads to a pairing pattern in the energy spectrum. In multivalley superlattices, the splitting of each pair can be shown to be a sinusoidal function of the width of the energy well or barrier.

The miniband energies decrease as the width of the well and barrier increases. Also, the lower the miniband energies are, the smaller their bandwidths become, due to higher barriers. The miniband energies versus different well and barrier widths are shown in Figs. 2.3 and 2.4. It should be noted from the figures that the miniband location is a strong function of the well width while the miniband bandwidth is a strong function of the barrier width. The minibands become discrete doublet energy levels as the barrier become thick enough in the quantum well limit.

B. Stepped well superlattice

Although Si and $\text{Si}_{1-x}\text{Ge}_x$ composites surfaces are chemically compatible, there is less than 4% lattice mismatch between the two materials. The strain induced from the lattice mismatch thus play an important role in determining the relevant band alignments between these materials. The band offsets for Si and $\text{Si}_{1-x}\text{Ge}_x$ have been studied by several workers.^{42,43} Van de Walle and Martin⁴² present the strain effects on the valence band offset using a self-consistent calculation based on the local density functional and *ab initio* pseudopotentials. Comparing their results with those of People⁴³ for a same strained

heterostructure of Si-Si_{0.5}Ge_{0.5} grown on a buffer layer of Si_{0.75}Ge_{0.25}, they give the valence band offset of 0.265 eV while People's gives a value of 0.3 eV. People⁴³ reports band alignments for coherently strained Si-Si_{1-x}Ge_x heterostructures on various substrates including Si_{1-y}Ge_y buffer layers, varying the fraction of Ge. The results are used in lining up a band diagram for a stepped well in this work. With using Si_{0.75}Ge_{0.25} as a middle well, which is the same material for the buffer layer and has an average lattice spacing between that of Si and that of Si_{0.5}Ge_{0.5}, the band line up is given in Fig.2.5. Because the energy gaps and valence band offsets have already been given for Si_{1-x}Ge_x epi- or buffer layer with various Ge contents, the band alignment could be achieved easily with an energy gap of 1 eV for Si_{0.75}Ge_{0.25}. Using Baslev's data,⁴⁴ the quartet-doublet splitting has also already been given in a few studies^{3,4} in which the same buffer layer is used. Since no strain-induced splitting arises between Si_{0.75}Ge_{0.25} epi- and buffer layers, Fig.2.5 can be completed to include the quartet-doublet splittings. The twofold bands(doublet; denoted with a solid line in Fig.2.5) are the longitudinal valleys with heavy effective masses along the growth direction with $k_{\parallel}=0$. The fourfold bands(quartet; denoted with a dashed line in Fig.2.5) are the transverse ellipsoids in the x-y plane with $k_{\parallel}=0$. No coupling is expected between the twofold and fourfold valleys since k_{\parallel} is conserved across the interface. Thus the well depths for the stepped-well are shown in Fig.2.5 as the distances between the twofold valleys. What should be mentioned here for obtaining the band alignment is that the equilibrium in-plane lattice constant for the epilayers is assumed the same for both layers of Si and Si_{0.5}Ge_{0.5} in order to share People's data.⁴³ It might not necessarily be the same, but it is expected that the difference should be extremely small if

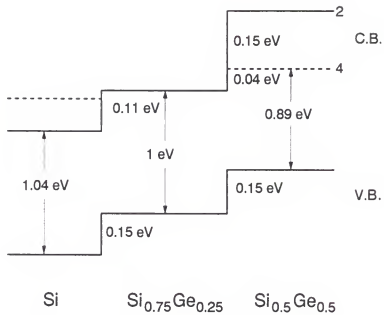


Fig. 2.5. Band line-up for a stepped well grown on $\text{Si}_{0.75}\text{Ge}_{0.25}$ buffer layer. The "2" refers to the two degenerate conduction band minima, and "4" refers to the four minima.

similar thicknesses are used for the two layers because another layer inserted between the two layers has the average Ge content, i.e., medium lattice constant.

The miniband structure for the stepped well superlattices is shown in Fig.2.6, varying the width of middle barrier. It is similar to the case of a square well superlattice with barrier width variation, which is shown in Fig.2.4.

C. Two-well coupling

The coupling of two quantum wells is found to have more energy levels allowed than does the single quantum well of the same dimension. The theoretical calculation of the minibands is shown in Fig.2.7 for a superlattice basis consisting of two square wells, one of the well widths is fixed and the other varied. Compared to Fig.2.2, it is clear that in the two-well case the minibands are mixed from those of its original wells. The two horizontal bands in the figure indicate the energy levels for a constant well width. While the four falling bands are the minibands of the variable well.

The cross points in Fig.2.7 are where the minibands of the two wells are aligned. The first cross point occurs when the varied well width is about 3 monolayers, where its only miniband is aligned with the upper miniband of the 12 monolayer well. The aligned bands have much larger bandwidth than the nonaligned bands which are bound states in nature, since the nonsymmetrical well acts as a barrier for the nonaligned minibands.

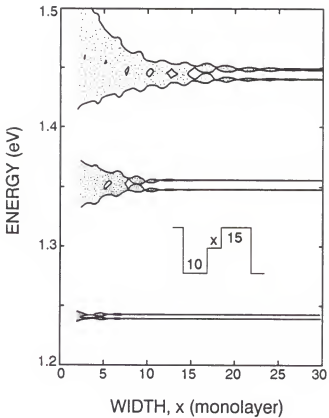


Fig. 2.6 The miniband energies versus middle barrier width. The well and higher barrier widths are fixed to 10 and 15 monolayers, respectively.

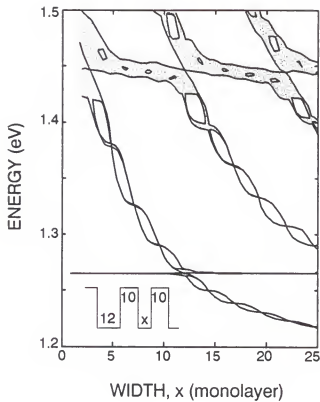


Fig.2.7. The miniband energies versus a well width. The first well, barrier, and the second barrier widths are fixed to 12, 10, and 10 monolayers, respectively.

2.4 Conclusion

The conduction band structures are presented for various Si/Si_{1-x}Ge_x superlattices using the transfer matrix method of Lee,⁶ which extended that of de Sterke and Hall⁴ to the general Hamiltonian (for Δ_1 bands). Variations of the miniband energies and the bandwidths are calculated as a function of the well or barrier width. The information for miniband energies given in this study should be useful for designing a band aligned superlattice (BAS), which has possible applications for a low dark current detector. The crisscross behavior due to the intervalley mixing effect of multivalley semiconductors is observed and explained.

CHAPTER 3

INTERSUBBAND OPTICAL ABSORPTION IN Si/Si_{1-x}Ge_x SUPERLATTICE

3.1 Introduction

Recently, intersubband optical absorption in Si/Si_{1-x}Ge_x superlattices has attracted attention because of the possibility of optoelectronic applications and the prospect that such structures may be integrated with conventional silicon integrated circuits.^{9,10} To take advantage of the Si/Si_{1-x}Ge_x superlattice detectors in current VLSI technology, the superlattices should be grown in the [100] direction and exhibit fairly large absorption coefficients for incident light. It has been reported that [100] Si/Si_{1-x}Ge_x superlattices are just as effective as GaAs/Al_xGa_{1-x}As superlattices for detection of infrared radiation.⁹⁻¹²

In this chapter the absorption coefficient in [100] growth direction is investigated with a Si/Si_{0.5}Ge_{0.5} superlattice structure. In previous studies of the absorption coefficient for Si/Si_{1-x}Ge_x heterostructures, a single wave function has been used to approximate the actual multicomponent envelope functions.¹¹⁻¹³ The approximation also neglects effects due to intervalley interference that would be present if the complete envelope functions are considered.¹² In those studies, the approximation was made to ease calculations and also to show the effect of an anisotropic effective mass on the selective optical absorption in the [100], [110], and [111] growth directions. Use of a single wave function approximation, however, can cause errors and even produce insufficient information for

the absorption coefficient since the effects due to intervalley interference are neglected. The complete multicomponent envelope functions are utilized here for determining the absorption coefficient and the results are compared to the single wave function predictions.

3.2 Conduction Band Structure

The energy band structure of Si/Si_{1-x}Ge_x superlattices is obtained with the envelope function approximation in which the complete form of the $\mathbf{k} \cdot \mathbf{p}$ Hamiltonian for Δ_1 bands is used. The parameters of zone-center energies and the momentum matrix elements are those given by Lee⁶ and the same connection rules at the interfaces are applied. In this study the Si/Si_{1-x}Ge_x superlattice with x=0.5 is chosen, for which the band offset of 0.3 eV is well established. For the wavelength range of interest for atmospheric communications (8-14 μm), a structure of the superlattice is selected which consists of a 15 monolayer Si well followed by a 5 monolayer Si_{0.5}Ge_{0.5} barrier. The desired wavelength could be attained using much thicker barrier layers. However, such a superlattice configuration is likely to have flatter energy subbands and consequently exhibit sharper absorption peaks on the incident photon energy. In this study, the more dispersed energy subbands in the 15×5 superlattice are considered to show more distinctive differences between the two cases of using the multicomponent envelope functions and single wave function.

It is generally agreed that photodetectors using intersubband transitions should have thick barriers in order to decrease the dark current, specially due to thermionic emission at zero or low electric field.²² This dark current could dominate the output

photocurrent since relatively thin barriers are considered in this study. However, this effect should be more severe in GaAs than Si because GaAs needs a much higher Fermi level than Si does in order to get the same doping concentration. In the $\text{Si}/\text{Si}_{1-x}\text{Ge}_x$ superlattice structure only the lower energy subband states are expected to be occupied by electrons at the low Fermi energy level which will be used in this study.

The calculated energy band structures of the $\text{Si}/\text{Si}_{0.5}\text{Ge}_{0.5}$ superlattice of interest are shown in Fig. 3.1. Due to intervalley interference, the conduction subbands yield doublets when the complete $\mathbf{k}\cdot\mathbf{p}$ Hamiltonian is taken into account for the multicomponent envelope functions. In the single wave function, on the other hand, the doublets are reduced to single subbands. Since the band structure around the conduction band minimum is the primary interest in this study, the values of the longitudinal effective masses and wave vectors at the energy minima for Si and $\text{Si}_{0.5}\text{Ge}_{0.5}$ are used in the case of the single wave function to minimize the difference with the bulk energy bands given by the full $\mathbf{k}\cdot\mathbf{p}$ Hamiltonian. The k_{\min} 's of 0.50 and 0.49, m 's of 0.92 and 0.90 are selected for Si and $\text{Si}_{0.5}\text{Ge}_{0.5}$, respectively.

The difference between the multicomponent envelope functions and the single wave function approach is pronounced in the charge densities of the wave functions at the same wave vector. The complete multicomponent envelope functions consist of rapidly varying carrier waves that are superimposed on slowly varying envelope functions. On the other hand, the single wave function has only a slowly varying envelope function. The charge densities of the conduction subbands are shown in Fig. 3.2. It should be noted that the intra-doublet transitions (e.g., 1 → 2 or 3 → 4, if the subbands are labelled

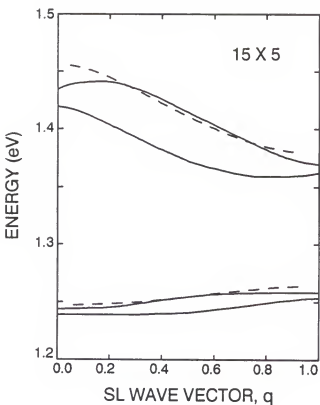


Fig.3.1. Band structure of $\text{Si}/\text{Si}_{0.5}\text{Ge}_{0.5}$ superlattice. The solid line are calculated from the multicomponent envelope functions and the dashed ones from a single wave function.

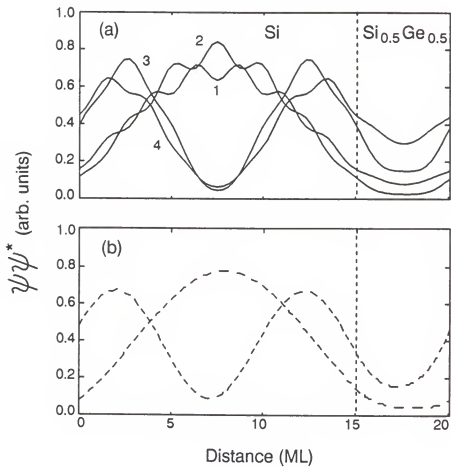


Fig. 3.2. The charge densities of (a) all four subband states obtained by the multi-component envelope function and of (b) approximated bands with a single wave function.

from lowest to highest energy in Fig. 3.1) are expected to have large transition strengths but the transition energies are very small. These transitions are not shown under the single wave function approximation in Fig.3.2 due to the reduction of the doublet to a singlet. The inter-doublet transitions in Fig.3.1 are expected to have similar transition strengths to those of the intersubband transitions in Fig. 3.2(b) since the coupling between the doublets is likely to be close to that between the single subbands. Note in this regard that the charge densities in Fig. 3.2(b) are almost averages of the doublet charge densities in Fig. 3.2(a).

3.3 Intersubband Absorption Coefficient

The momentum matrix elements of the wave functions should necessarily be given to calculate the absorption coefficients for intersubband transitions. The absorption coefficient α is defined as $\hbar\omega$ times the number of transitions per unit volume and time, divided by the incident energy flux⁴⁵

$$\alpha = \frac{2}{V} \sum_{m,n,q} \sum \left\{ 2\hbar\omega W_{mn} / \eta c \epsilon_0 \omega^2 A_o^2 \right\} \quad (3.1)$$

Here η is the refractive index, ϵ_0 the permittivity and A_o is the amplitude of the radiation field. The factor 2 in front of the summations accounts for a possible change of spin during absorption. The rate of intersubband transition W_{mn} from the initial state Ψ_m to the final state Ψ_n is expressed as

$$W_{mn} = \frac{2\pi}{\hbar} |\langle \Psi_n | H' | \Psi_m \rangle|^2 (f_m - f_n) \delta(E_m - E_n + \hbar\omega) \quad (3.2)$$

where f represents the Fermi-Dirac distribution function. The interaction Hamiltonian H' is expressed as a perturbation in the total Hamiltonian of the superlattice due to optical radiation and is given by

$$H' = -\frac{e}{m_o} \mathbf{A} \cdot \mathbf{p} \approx -\frac{e}{2m_o} e^{i\mathbf{q} \cdot \mathbf{r} - i\omega t} \mathbf{\epsilon} \cdot \mathbf{p} \quad (3.3)$$

Therefore, the matrix element of the interaction Hamiltonian can be approximated as

$$\begin{aligned} \langle \Psi_n | H' | \Psi_m \rangle &\approx \frac{eA_o}{2m_o} \langle \Psi_n | \mathbf{\epsilon} \cdot \mathbf{p} | \Psi_m \rangle \\ &= \frac{eA_o}{2m_o} [\langle u_c | \mathbf{\epsilon} \cdot \mathbf{p} | u_c \rangle \langle F_n | F_m \rangle + \langle u_c | u_c \rangle \langle F_n | p_z | F_m \rangle] \end{aligned} \quad (3.4)$$

where the u 's and F 's are the Bloch and envelope parts of the wave functions, respectively. The last expression is possible since the spatial dependence of the envelope function within a unit cell can be neglected. Only the second term of the last expression is non-zero for both cases of the complete and simplified calculations. It is more obvious for the case of single wave function approximation that the first term should be zero because of the orthogonality of the envelope functions. With a term $\langle \Psi_n | \mathbf{\epsilon} \cdot \mathbf{p} | \Psi_m \rangle$ denoted as P_{mn} , the

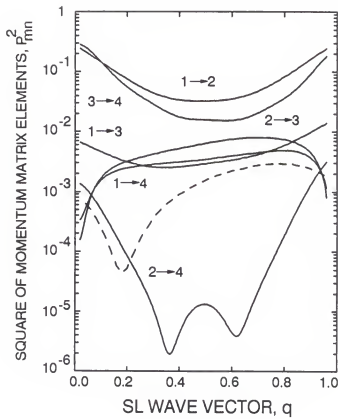


Fig.3.3. The square of momentum matrix elements for all the intersubband transitions as a function of the superlattice wave vector.

dependence of P_{mn}^2 on the superlattice wave vector q for all the possible transitions is shown in Fig. 3.3. The dashed curve represents the result obtained by the single wave function approximation. Although the dashed curve shows a shape similar to the average of the P_{mn}^2 curves for the inter-doublet transitions, the absolute values of the dashed curve are at least 5 times smaller than the highest value of P_{mn}^2 for the inter-doublet transitions, which occur at the superlattice Brillouin zone edge of the $1 \rightarrow 3$ transition. Since the absorption coefficient is directly proportional to the square of momentum matrix elements, P_{mn}^2 , its estimated value would be much lower if the single wave function approximation is used.

Using the aforementioned equations the absorption coefficient is given by

$$\alpha = \frac{e^2 m^* k_B T}{\pi n_o^2 \eta c \epsilon_o \omega \hbar^2} \int_0^{\pi/L} \ln \left[\frac{1 + \exp\left(\frac{E_F - E_m}{k_B T}\right)}{1 + \exp\left(\frac{E_F - E_n}{k_B T}\right)} \right] |< \Psi_n | \mathbf{e} \cdot \mathbf{p} | \Psi_m >|^2 \frac{\Gamma / 2\pi}{[\hbar \omega - E_{mn}(q)]^2 + \Gamma^2 / 4} dq. \quad (3.5)$$

where E_F is the Fermi energy and Γ is a broadening parameter in the normalized Lorentzian function. As shown in Fig. 3.3, the momentum matrix elements are a function of the superlattice wave vector and thus the term is introduced into the integral in Eq.(3.5). With thicker well and barrier layers, however, the momentum matrix elements become constant over the entire range of superlattice wave vector q because the subbands tend to be flat.

The absorption coefficient for all transitions is calculated numerically for 300 K. In Fig.3.4, the absorption coefficient α is plotted for the incident photon energy with

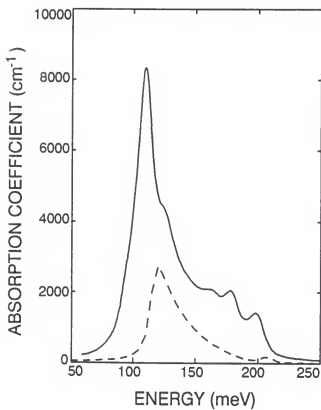


Fig.3.4. Comparison of the intersubband absorption coefficients: multicomponent wave functions(solid curve) ; single wave function(dashed curve).

polarization perpendicular to the well, taking into account all the subband states as a function of superlattice wave vector. With the Fermi energy at the conduction band minimum of the Si well, for which the electron density is about $4.6 \times 10^{17} \text{ cm}^{-3}$ and the broadening parameter Γ is 8 meV, the absorption coefficients are compared for both the rigorous and approximate calculations. As expected from Fig. 3.3, the absorption coefficient by the approximate, single wave function turns out to be about 5 times lower and does not exhibit all the transition peaks that should be present when the multicomponent envelope functions are used.

The absorption coefficient given here with the multicomponent envelope functions is of the same order of magnitude as that obtained by Chang *et al.*²⁹ from a calculation based on four antibonding orbitals. However, their absorption coefficient is for the flat energy levels arising from a sufficiently wide barrier.

The absorption coefficient α is a function of temperature, as shown in Eq. (3.5). At 300 K the electron density N in the superlattice can be obtained by

$$N = \sum_i N_i \quad (3.6a)$$

$$N_i = \frac{m^* k_B T}{\pi L \hbar^2} \ln \left[1 + \exp \left(\frac{E_F - E_i}{k_B T} \right) \right] \quad (3.6b)$$

where E_i is the i th quantized subband energy level. However, it should be noted that at lower temperatures ($T < 77 \text{ K}$), the exponential term in the logarithm in Eq. (3.6b) becomes large compared to unity and so Eq. (3.6b) reduces to

$$N_i = \frac{m^*}{\pi L \hbar^2} (E_F - E_i). \quad (3.7)$$

Assuming that most of the carriers populate in the two lowest doublets, the Fermi level can be calculated from

$$E_F = \frac{(E_0 + E_1) + N / D}{2}, \quad (3.8)$$

where the subscript 0 (1) refers to the ground (first ground) state and D is the density of states. From the above equation, E_F of about 100 meV is found at a temperature of 77 K for the carrier density $N = 4.6 \times 10^{17}$ cm⁻³. Using the Fermi energy, one can obtain the absorption coefficient at the temperature. It is estimated in this study that the value of the absorption coefficient at 77 K would be 12 times higher than that at 300 K.

3.4 Summary

The absorption coefficient for intersubband transitions in Si/Si_{1-x}Ge_x superlattices have been calculated using multicomponent envelope functions. The results are compared with those obtained by a single wave function approximation. Large differences in the absorption coefficient were found between the two cases. The differences are analyzed in terms of the charge densities of the wave functions and the momentum matrix elements for the intersubband transitions involved. It is found that the absorption coefficient

estimate is much lower and most of the transition peaks are absent when the single wave function approximation is used.

CHAPTER 4
ELECTRIC FIELD EFFECT ON INTERSUBBAND OPTICAL ABSORPTION IN A
 $\text{Si}/\text{Si}_{1-x}\text{Ge}_x$ SUPERLATTICE

4.1 Introduction

In recent years, intersubband optical transition in $\text{Si}/\text{Si}_{1-x}\text{Ge}_x$ superlattices has attracted attention because of its unique possibility to detect normally incident light.^{11-13,29} The allowed absorption at normal incidence is due to the anisotropic effective mass of Si in [110] and [111] directions. Nevertheless, the absorption in [100] direction should still be very important to take advantage of [100]-grown $\text{Si}/\text{Si}_{1-x}\text{Ge}_x$ superlattice detectors in current VLSI technology. Even though the optical absorption in [100] direction is zero at normal incidence, it could be circumvented with gratings to increase the coupling efficiency of normal illumination as is usually done with $\text{GaAs}/\text{Al}_x\text{Ga}_{1-x}\text{As}$ detectors.

The effect of an external electric field upon electronic states(the Stark effect) in single or multiple quantum-well structures has been studied in the literature.⁴⁵⁻⁵⁰ Of particular interest were the field-induced changes in the energy-level structure and the localization of the charge density associated with the Stark resonances at the bottom of the conduction band. These studies dealt with the III-V semiconductor heterostructures whose conduction band structure could be described by the simplest one-dimensional effective-mass equation. Early attempts to model the effect of electric field were based on approximate techniques such as perturbation and variational methods.^{51,52} Recent studies,

however, gave an exact solution described by the Airy functions for the structures.^{47-49,53} For a heterostructure of Si and $\text{Si}_{1-x}\text{Ge}_x$, the Airy function solution does not satisfy if the full Brillouin zone description for electronic structure of the indirect band gap materials is taken into account. This is because the lowest conduction band in the materials belongs to the Δ_1 bands for [100] direction, which are given as a 3×3 matrix. In this work, the transfer matrix technique is used to examine the effect of an electric field. The electric potential is approximated with a series of piece-wise constant potential steps in this study. The transfer matrix technique offers the versatility of allowing any type of external potentials to be applied, when compared to the variational method or the Airy function approach, in solving the Schrödinger equation for quantum-well structures under applied electric fields. The Airy functions are sometimes limited by numerical instabilities since they must be approximated by power series expansions. In particular they apply only to cases of linear potentials and cannot be adapted to a system with coupled nonlinear band structures. Variational methods are capable of handling nonlinear potentials, but as with the Airy functions, are not easily modifiable for use in multiple quantum-well potentials.

When an electric field F is applied along the growth axis, the superlattice resonance condition is turned off. Thus, an energy miniband of the superlattice splits into a series of discrete levels (Wannier-Stark ladders) and they become misaligned by eFd . The consequences of this effect have been examined theoretically by Bleuse et al⁵⁴. As the tunneling probability decreases due to the misalignment, the eigenstates become localized over a few adjacent quantum wells. All the studies on the Wannier-Stark ladder formation have concentrated on the interband transition from valence to conduction bands so far.⁵⁴⁻⁵⁸

Hole states are coupled weakly and become fully localized under rather low electric fields because of their large effective mass, while the large spartial extent of the electron wave functions remains. Strength of the interband transition has been obtained from a localized hole state to unlocalized electron states for both inter and intra-well recombination transitions.⁵⁴⁻⁵⁷ This might also happen in intersubband transitions between the conduction sublevels since the lowest energy level becomes localized much faster than the upper level does as the electric field increases. The chief aim of this paper is to elucidate the electric field effect on conduction intersubband transitions in a Si/Si_{1-x}Ge_x superlattice, which has not yet been explored.

The optical absorption for intersubband transitions between the Wannier-Stark states in a Si/Si_{1-x}Ge_x superlattice under electric fields is reported here for the first time. Full spectra of the absorption coefficient are given at various electric fields. The result shows a possibility of utilizing the superlattice as a waveguide material. The adjustability of the absorption coefficient with applied electric field has an important potential application in providing adjustable phase modulation of a light beam for the infrared photon energy range of 100-300 meV.

4.2 Theory

Consider a superlattice with its period consisting of a Si well and a Si_{0.5}Ge_{0.5} barrier. In anticipation of the envelope function approach to be used for the superlattice, the conduction-band structure of the constituent materials is taken up first. For the [100]

direction being considered, the Δ_1 bands to which the lowest conduction band of bulk Si belongs are given as the eigenvalues of the following matrix:⁴¹

$$\begin{bmatrix} E_{15} + k_x^2 & Tk_x & T'k_x \\ Tk_x & E_1'' + k_x^2 & 0 \\ T'k_x & 0 & E_1' + k_x^2 \end{bmatrix}. \quad (4.1)$$

where E_{15} , E_1'' , and E_1' are the values of the energy bands at the Γ point in increasing order, and the T and T' are the momentum matrix elements, for which expressions are given in the literature.^{5,41} The $\mathbf{k}\cdot\mathbf{p}$ Hamiltonian given by Eq.(4.1) can be used to write the differential equations for the envelope functions, the solutions of which lead to the elements of transfer matrices. The transfer matrix technique can then be used to arrive at the conduction bands of the superlattices. The connection rules used are that the envelope functions are continuous over an interface and that $(-1 + T'^2/\gamma)dF_i/dx$ are also continuous, where the subscript i is for the envelope functions F . Here γ is given^{6,60} by

$$\gamma = (E - E_1' - k_1^2)(E - E_1' - k_2^2) / (E_1' - E_1'') \quad (4.2)$$

where k_1 and k_2 are the physically valid wave vectors for the constituent bulk materials, which are Si and Ge.

For consistency, the momentum matrix elements T and T' in Eq.(4.1) should be the same for the two constituent materials of the superlattice. Although the values for one constituent material have been used for the other in direct semiconductors as in

GaAs/Al_xGa_{1-x}As in the past,³⁹ average values of T and T' for Si and Ge are used in this work. This necessitates adjustments of the energy levels of the zone-center states so as to represent properly the lowest Δ_1 band in both Si and Ge. Average values between Si and Ge are used for the zone-center energies of Si_{0.5}Ge_{0.5}. The conduction-band offset between Si and Si_{0.5}Ge_{0.5} on Si_{0.75}Ge_{0.25} is well established,^{4,5} which is 0.3 eV. Details are given in the chapter 2 or elsewhere.⁶ The wave vectors for the superlattice can be obtained by the eigenvalues of the overall transfer matrix.

When an electric field is applied to a superlattice the same calculation scheme can be followed by approximating the tilted electric potential with a series of piece-wise constant potential steps as shown in the magnified circle of Fig.4.1. Here a finite length superlattice in which 11 wells are sandwiched alternatively by 12 barriers with infinite potentials at both ends is considered. It is well known that the resonance condition of the superlattice energy band is turned off when an electric field is applied along the growth axis and the energy levels of consecutive multiple quantum wells become misaligned by eFd where d is the length of superlattice unit cell. As a result of the misalignment the tunneling probability decreases drastically and the eigenstates tend to localize over a few adjacent quantum wells. With the reduced coherence length of the eigenstates under an electric field, it is assumed that the 11 period finite superlattice is enough to simulate the infinite length superlattice. In our calculation, instead of applying the Bloch condition for the superlattice energy band, a boundary condition that the envelope functions vanish at both ends is used for the finite superlattice with an electric field since infinite energy barriers are assumed at the ends. It should be noted here that due to the presence of the electric field

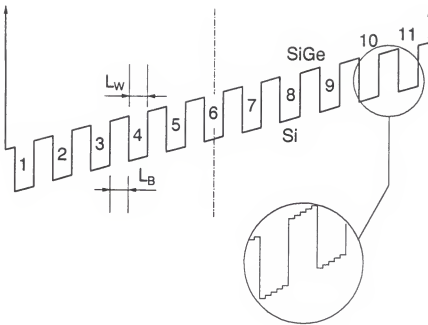


Fig. 4.1. Multiple quantum well structure used in calculation. Typical potential structure used in the transfer matrix technique is shown in a magnified circle.

the total potential of a superlattice goes from $-\infty$ to ∞ , so that the system does not have true bound states. However, within each quantum well, there are quasibound states which have sufficiently long lifetimes to be observed by optical measurements. The assumption of infinite barriers at both ends enables to find the approximate energies and wave functions of these quasibound states. On the other hand, it also could result in a weak distortion of the wave functions far away from the center of the multiple quantum well of interest, and a small shift of energies for the quasibound states. The error caused by imposing the artificial boundary conditions of infinite energy barrier at both ends should become smaller as the larger number of period for the finite superlattice is used. It is expected that the 11 period finite superlattice should be enough to give the useful informations for the same dimension superlattice with infinite period, with reasonable accuracy despite any error which could originate from the artificial boundary conditions.

For the wavelength range of interest for atmospheric communications(8-14 mm), a structure of the superlattice is selected, which consists of 15 monolayers of Si well followed by 5 monolayers of $\text{Si}_{0.5}\text{Ge}_{0.5}$ barrier, so that the structure has transitions in the wavelength range of interest. The desired wavelength could be attained using much thicker barrier layers. In this case, however, the eigenstates of a structure with thicker barrier layers tend to completely localize even at a very low electric field so that the coherence length is too short. Thus, rather thin wells and barriers are chosen in this study. We consider the linearly tilted potential formed by an applied electric field as a series of constant piece-wise potential steps.^{61,62} The approximation is possible due to the discrete nature of crystal growth, so that the smallest possible division is the length of a monolayer.⁶³ Here,

7 steps in Si well layers and 3 steps in $\text{Si}_{0.5}\text{Ge}_{0.5}$ barrier layers are used. First the transfer matrix in each divided layer is found, then the total transfer matrix is obtained by multiplying all these transfer matrices and connecting them with the appropriate connection rules stated earlier. Finally the energy levels are obtained by applying the boundary conditions of vanishing envelope functions at both ends.

At zero electric field the two lowest doublet bands of the 15×5 superlattice are obtained as shown in Fig.4.2. The lowest doublet miniband ranges from 1.24 to 1.26 eV and the second doublet is dispersed in the energy range from 1.36 to 1.44 eV. From Fig.4.2 the strongest transition could be expected at around the superlattice zone edge where almost direct optical transition is possible. As soon as an electric field turns on, the resonance condition collapses and the superlattice miniband breaks into the Stark energy levels unavoidably. The calculated conduction eigenstates in an 11 well 15×5 superlattice versus electric field are shown in Fig.4.3. At zero field the energy ranges of the two lowest conduction minibands turn out to be the same as those in Fig.4.2. Each miniband breaks into 11 Stark energy doublets and the gaps between doublets become wider as the applied electric field increases. Here it can be seen that for low electric fields the variation of energy levels with field is slower than that for high fields greater than about 30 kV/cm for lower levels and 80 kV/cm for higher levels. This is a consequence of higher wave function localization for higher electric fields.

It should be noted here that crossings between the lower and higher subbands are anticrossings in reality because there is no reason why the matrix elements between the

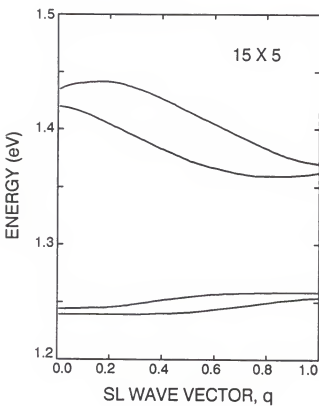


Fig 4.2. Conduction band structure of a Si/Si_{1-x}Ge_x superlattice which is composed of 15 monolayers of Si well followed by 5 monolayers of Si_{1-x}Ge_x barrier material.

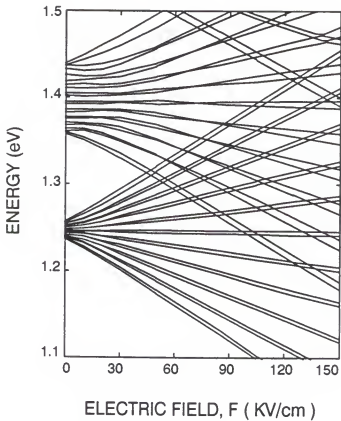


Fig.4.3. Variation of resonance energy with electric field for conduction electrons;
Each (mini)band at zero field splits into 11 doublet sublevels under an
electric field.

lower and higher subbands should all be zero.⁶⁴ The broadening due to the interaction between those subbands, however, is too small to be noticed in the anticrossings in Fig.4.3.

Figure 4.4 shows the evolution of wave function localization with electric field, that is to say, the charge density versus length of the finite superlattice for various electric fields. The charge densities are calculated at the lowest energy level in the center well (6th well). At zero field the wave function is resonant and Bloch condition holds. The lowest states become more localized as the electric field increases and eventually the states become almost completely localized at an applied field of 50 kV/cm. While the lowest states are completely localized at above 50 kV/cm, the second subband states are not strongly localized until very high field is reached. As shown in Fig.4.5, even at 150 kV/cm the center well does still interact with adjacent wells. In the bottom of Fig.4.5 a completely localized charge density of the lowest state is shown. Here 6-1 represents the sixth well and the first (lowest) energy level, 3-2 the third well and the second energy level, and so forth. At 150 kV/cm the second lowest state in the sixth well is very close to the third state in the first well as can be seen in Fig.4.3. This is why there exists charge density in the first few wells in the third figure from the top of Fig.4.5, which is numbered by 6-2.

4.3 Intersubband Optical Transition

The absorption coefficient α is defined as $\hbar\omega$ times the number of transitions per unit volume and time, divided by the incident energy flux,⁴⁵

$$\alpha = \frac{2}{V} \sum_{m,n} \sum_{k,k'} \left\{ 2\hbar\omega W_{mn} / (\eta c \epsilon_0 \omega^2 A_o^2) \right\}. \quad (4.3)$$

Here η is the refractive index, ϵ_0 the permittivity and A_o is the amplitude of the radiation field. The factor 2 in front of the summations accounts for a possible change of spin during absorption. The rate of intersubband transition W_{mn} from the initial state Ψ_m to the final state Ψ_n is expressed as

$$W_{mn} = \frac{2\pi}{\hbar} | \langle \Psi_n | H' | \Psi_m \rangle |^2 (f_m - f_n) \delta(E_m - E_n + \hbar\omega) \quad (4.4)$$

where f represents the Fermi-Dirac distribution function. The interaction Hamiltonian H' is termed as a perturbation in the total Hamiltonian of the superlattice due to optical radiation and given by

$$H' = -\frac{e}{m_o} \mathbf{A} \cdot \mathbf{p} \approx -\frac{e}{2m_o} e^{i\mathbf{q}\cdot\mathbf{r}-i\omega t} \mathbf{e} \cdot \mathbf{p} \quad (4.5)$$

where \mathbf{A} is the vector potential, \mathbf{e} is the polarization vector, \mathbf{q} is the wave vector for incoming optical radiation, and \mathbf{p} is the momentum vector of the electron in the crystal. The matrix element of the interaction Hamiltonian can be approximated as

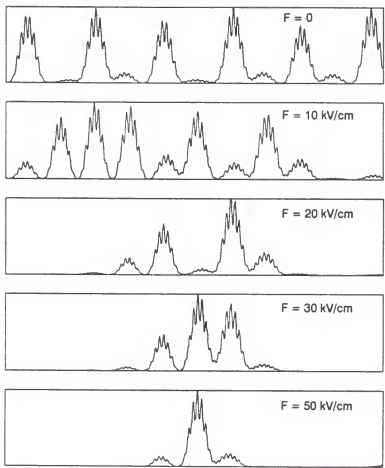


Fig.4.4. Variation of charge density for the lowest state confined in a well located in the middle with field.

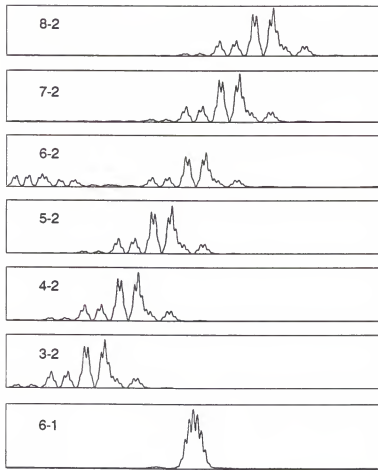


Fig.4.5. Charge densities for the second lowest state (6 boxes from the top) and for the lowest state(bottom), confined in a well located in the middle, all at 150 kV/cm.

$$\begin{aligned} <\Psi_n|H'|\Psi_m> &= \frac{eA_o}{2m_o} <\Psi_n|\boldsymbol{\epsilon} \cdot \mathbf{p}|\Psi_m> \\ &= \frac{eA_o}{2m_o} [<u_c'|\boldsymbol{\epsilon} \cdot \mathbf{p}|u_c><F_n|F_m> + <u_c'|\mathbf{u}_c><F_n|\mathbf{p}_z|F_m>] \quad (4.6) \end{aligned}$$

where the u 's and F 's are the Bloch and envelope parts of the wave functions, respectively. The last expression is possible since the spatial dependence of the envelope function with a unit cell can be neglected. The first term of the last expression should be zero because of the orthogonality of the envelope functions. Using the aforementioned equations the absorption coefficient is given by

$$\alpha = \sum_m \sum_n \frac{e^2 m^* k_B T}{\pi m_o^2 \eta c \epsilon_o \omega \hbar^2 L} \ln \left[\frac{1 + \exp\left(\frac{E_F - E_n}{k_B T}\right)}{1 + \exp\left(\frac{E_F - E_m}{k_B T}\right)} \right] |<\Psi_n|\boldsymbol{\epsilon} \cdot \mathbf{p}|\Psi_m>|^2 \frac{\Gamma / 2}{[\hbar \omega - E_{mn}]^2 + \Gamma^2 / 4} \quad (4.7)$$

where E_F is the Fermi energy and Γ is a broadening parameter in normalized Lorentzian function and L is the total length of the 11 period finite superlattice.

The absorption coefficient for intersubband transitions numerically for 300K is calculated. The absorption coefficient α for the incident photon energy with polarization perpendicular to the wells for a few different electric fields is plotted in Fig.4.6. In the calculation the Fermi level energy of 0 mev, at which the electron density is about 4.6×10^{17} cm⁻³, and the broadening parameter Γ of 8 meV are used. At non-zero electric field the

15×5 infinite superlattice is considered as a finite length superlattice instead, which has 11 periods of the superlattice unit cell, assuming that the interaction between wells is not appreciable beyond 11 wells under the electric field being considered.

When no electric field is applied, superlattice minibands are formed and their dispersions on the superlattice wave vector q are relevant to the absorption coefficient. With the knowledge of the superlattice band structure the absorption coefficient at zero field is given by

$$\alpha = \frac{e^2 m' k_B T}{\pi n_o^2 \eta c \epsilon_o \hbar^2} \int_0^{\pi/d} \ln \left[\frac{1 + \exp\left(\frac{E_F - E_m}{k_B T}\right)}{1 + \exp\left(\frac{E_F - E_n}{k_B T}\right)} \right] |<\Psi_n| \mathbf{e} \cdot \mathbf{p} |\Psi_m>|^2 \frac{\Gamma / 2\pi}{[\hbar\omega - E_{mn}(q)]^2 + \Gamma^2 / 4} dq. \quad (4.8)$$

Because the momentum matrix element is a function of the superlattice wave vector, the term, $|<\Psi_n| \mathbf{e} \cdot \mathbf{p} |\Psi_m>|^2$ should be integrated over the superlattice wave vector q as shown in Eq.(4.8). The transition energy which is also dependent on the wave vector q is substituted for E_{mn} . The zero-field absorption coefficient is shown at the top of Fig.4.6 along with the coefficients at different electric fields. The resonance condition that stands at zero field collapses and the discrete Stark levels show up as soon as an electric field turns on. It should be understood that above a certain electric field the lowest energy state is completely localized while the upper energy states are not, as shown in Figs.4.4 and 4.5. This is the similar situation that arises in an interband transition from valence to conduction

band, since localization of hole eigenstates is much more severe than that of electron states under the electric field. As mentioned earlier, for the interband transition the Wannier-Stark ladder forms under an electric field due to the localization of the eigenstates of holes and electrons. For the intersubband transition between conduction sublevels which is considered here, localization of the lower eigenstates results in a similar Wannier-Stark ladder. As shown in Fig.4.6, at 30 kV/cm a number of transition peaks are resolved from the zero-field spectrum as a result of the Wannier-Stark ladder formation. As the electric field increases, the energy spacings between the ladders also increase and thus the resolved peaks become separated further. Most of the peaks in the absorption coefficient spectra in Fig.4.6 represent interwell transitions until the electric field reaches at 80 kV/cm. The intra-well transition, a transition between the energy sublevels confined in the same well, shows up at electric fields above 80 kV/cm. The intra-well transition is found at a photon energy of around 150 meV which is the average energy difference between two minibands shown in Fig.4.2. The late appearance of the intra-well transition at high field could be understood as being similar to the case for interband transitions, in which all the interband transitions involving recombination of a hole and an electron localized in the same well occur at high field. It is for this reason that single quantum well calculations show the high-field energy dependence of interband or intersubband transitions in multiple quantum well structures. The results shown in Fig.4.6 resemble the photocurrent spectrums which have been given by Agullo-Rueda et al.⁵⁶ and Dignam et al.⁵⁸ with a superlattice formed by sixty periods of alternating GaAs and Al_{0.35}Ga_{0.65}As layers.

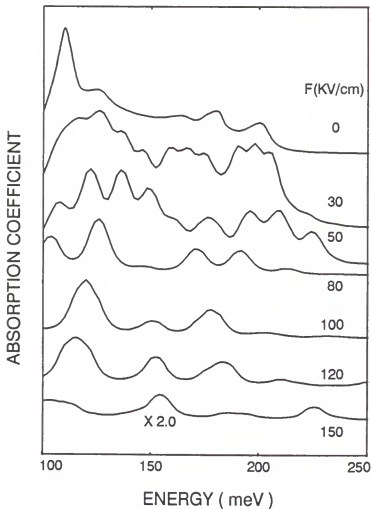


Fig.4.6. Calculated absorption coefficient spectra for a 15×5 Si/Si_{0.5}Ge_{0.5} superlattice at 300K.

It should be noted that the Stark shift is also seen in Fig.4.6. The Stark shift in quantum-well intersubband transitions was first observed by Harwit and Harris.⁶⁵ When an electric field is applied, the conduction band diagram tilts as shown in Fig.4.1. As the electric field increases, the lowest state decreases in energy as it sinks into the triangular potential formed by the bottom of the well and energy barrier. The higher energy states see the same potential in the well but they are less affected. The applied field thus causes an increase in the energy difference and therefore an increase in the photon energy necessary to excite an electron. In Fig.4.6, the peak for intra-well transition, which is shown at a photon energy slightly below 150 meV at 80 kV/cm, shifts to about 155 meV at 150 kV/cm. This Stark shift for intersubband transition in a quantum well is observed at high electric fields since the intra-well transition dominates only at high fields.

The calculated absorption coefficient is found in the range of about 3000 cm⁻¹ at its highest peak which of course depends on the electric field. In Fig.4.6 all the absorption coefficient spectra obtained in our calculation have the same scale except the bottom one which is scaled up by a factor of two, even though the values are not included in the figure.

4.4 Conclusion

The Wannier-Stark localization has been theoretically studied for conduction subbands in a Si/Si_{0.5}Ge_{0.5} superlattice. Full spectra of the absorption coefficient for intersubband infrared transitions have been presented, showing an existence of the Wannier-Stark ladders. It is observed that the Stark energy levels shift to the shorter photon wavelength for intersubband transitions as the electric field increases. The typical

Stark energy levels have been obtained with variation of electric field. Due to intervalley interference, however, each Stark level turns to be a doublet since the multicomponent envelope functions are considered in this study. The presented electro-optical effect on the superlattice due to electric field presented here should provide useful information for designing new modulators operated in the infrared range.

CHAPTER 5

IMPACT IONIZATION COEFFICIENT AND ENERGY DISTRIBUTION FUNCTION IN POLAR AND NONPOLAR SEMICONDUCTORS

5.1 Introduction

Impact ionization is an important process in semiconductor devices, in particular in avalanche photodetectors, and devices operating under high electric field, e.g., metal-oxide-semiconductor field-effect transistors (MOSFETs) in very large scale integrated circuits where the impact ionization is important source of device degradation.

Wolff⁶⁶ is perhaps the first who put forward a diffusion model for impact ionization with an argument that electrons gain energy gradually due to many collisions. Wolff's model is likely to dominate at very high electric fields where the average electron energy is comparable to the ionization threshold energy. Shockley's model⁶⁷, often referred to as the lucky electron model, presumes that only those few electrons lucky enough to avoid collisions gain sufficient energy from the field for the ionization. These lucky electrons could be characterized by their ballistic movements. This ballistic movement is expected to be dominant at low electric fields where the electron energy is very low compared to the ionization threshold energy.

The most widely used model, due to Baraff⁶⁸, reduces to Shockley's model in the low field range while it converges to Wolff's model in the high field limit. Recently, Ridley^{69,70} has extended Shockley's lucky electron model by making a distinction between

the rates of momentum and energy relaxation. This "lucky drift" model is intermediate between Shockley's ballistic state and Wolff's equilibrium state. All these models, however, assume that the mean free paths for scatterings are constant and independent of energy. In general, the mean free paths do depend on energy. Furthermore, these models do not give the exact form of the energy distribution function.

Perhaps the first attempt for energy dependent results is that by Keldysh⁷¹ who solved the Boltzmann transport equation on the basis of an assumed form for the symmetric part of the energy distribution function. Chen and Tang⁷² have provided an explicit expression for the energy dependent mean free path that is required for the use of Keldysh's results.

In this chapter, I solve the Boltzmann transport equation with a technique that has been developed by Nag⁷³. Full account is taken of all major scattering mechanisms, including intervalley optical phonon scattering. A distinction is made between polar and nonpolar optical phonon scattering, which has not been taken into consideration in previous studies where the energy dependency was included.⁷⁴

Development of the Boltzmann transport equation is given in Sec.5.2. Energy distribution functions and impact ionization coefficients for both polar and nonpolar semiconductors are then obtained in Sec.5.3. Comparisons with experimental results from nine different sources are given in Sec.5.4.

5.2 The Boltzmann Transport Equation

The classical theory of carrier transport processes in semiconductors is based on the Boltzmann transport equation. The Boltzmann equation is in the form of an integro-differential equation, and analytical solution of which is almost impossible to obtain. A variety of approximate methods have been developed to solve the equation for the transport coefficients. In general, the Boltzmann transport equation with steady field can be expressed as follows:

$$\left(\frac{F}{\hbar} \right) \cdot \nabla_k f = \frac{\partial f}{\partial t} \Big|_{\text{collision}} \quad (5.1)$$

where f denotes the distribution function of electrons, which is to be obtained from the equation. When the electron distribution is expressed in spherical harmonics with the direction of field as the polar axis, an approximate form of the solution is

$$f(k) = f_0(E) + k \cos \theta f_1(E) \quad (5.2)$$

with the series terminating at the second term. The distribution function can then be substituted into Eq.(5.1). Using Eq.(5.2) in both sides of the transport equation, Eq.(5.1) and equating the symmetric and asymmetric terms, f_0 and f_1 , respectively, yields

$$\frac{eF}{\hbar} \left(f_1(E) + k_x \frac{\partial f_1}{\partial E} \frac{\partial E}{\partial k_x} \right) = \frac{\partial f_0}{\partial t} \Big|_{\text{collision}} \quad (5.3)$$

$$\frac{eF}{\hbar} \frac{\partial f_0}{\partial E} \frac{\partial E}{\partial k_x} = k_x \frac{\partial f_1}{\partial t} \Big|_{\text{collision}} \quad (5.4)$$

Here I have set the component of the electron wave vector in the direction of the force on the electron, i.e., $k \cos \theta$ equal to k_x . The collision integral, $(df_0/dt|_{\text{collision}})$, which is the rate of variation of the symmetric part of $f(\mathbf{k})$ due to collision, can be obtained analytically under a few simplifying assumptions for various scattering collisions. On the other hand, the term $(df_1/dt|_{\text{collision}})$, which gives the variation of the asymmetric part of $f(\mathbf{k})$ due to collision, may be simplified to $(-k_x f_1/\tau_i(E))$ by the relaxation time approximation. The frequency of relaxation collisions as a function of the electron energy, which is the inverse of relaxation time τ_i , can be obtained from Tables 5.1 and 5.2. With the relaxation approximation, one may eliminate f_1 and combine Eqs.(5.3) and (5.4), resulting in

$$\frac{\partial f_0}{\partial t} \Big|_{\text{collision}} = -\frac{2}{3} \frac{(eF)^2}{m^*} E^{-\frac{1}{2}} \frac{d}{dE} \left(E^{\frac{3}{2}} \tau_i(E) \frac{\partial f_0}{\partial E} \right) \quad (5.5)$$

The above equation may be solved analytically for elastic and randomising collisions such as acoustic phonon scattering, and also for optical phonon scatterings with some simplifying assumptions. It is known that several scattering processes are effective

Table 5.1. Phonon scatterings^a

momentum relaxation times	collision intervals
acoustic phonon scattering:	$\tau_{ac} = \tau_{arm} w^{-\frac{1}{2}}$ $\left. \frac{\partial f_0}{\partial t} \right _{iac} = \frac{1}{\tau_{iac}} w^{\frac{1}{2}} \left[w \frac{d^2 f_0}{dw^2} + (w+2) \frac{df_0}{dw} + 2f_0 \right]$
nonpolar optical phonon scattering ^b	$\tau_{opm}^{-1} = \frac{\sqrt{2} m^{*\frac{3}{2}} (kT_L)^2 E_1^2}{\pi \rho \hbar^4 C_l^2}$ $\frac{1}{\tau_{opm}} = \frac{\sqrt{2} m^{*\frac{3}{2}} (kT_L)^2 E_1^2}{\pi \rho \hbar^4}$
	$\left. \frac{\partial f_0}{\partial t} \right _{op} = \frac{1}{\tau_{ope}} w^{-\frac{1}{2}} [f_0 + w \frac{df_0}{dw} + \frac{2n_0 + 1}{2} \frac{\hbar \omega_0}{kT_L} (\frac{df_0}{dw} + w \frac{d^2 f_0}{dw^2})]$ $\tau_{ope}^{-1} = \frac{(2m^*)^{\frac{3}{2}} D_0^2 (kT_L)^{\frac{1}{2}}}{4\pi \hbar^3 \rho w_0} (2n_0 + 1)$ $\frac{1}{\tau_{ope}} = \frac{D_0^2 m^{*\frac{3}{2}} (kT_L)^{-\frac{1}{2}}}{\sqrt{2\pi\rho\hbar^2}}$

Table 5.1 continued

Polar optical phonon scattering	$\tau_{pop} = \tau_{popm} w^{\frac{1}{2}}$	$\left \frac{\partial f_0}{\partial \tau} \right = \frac{1}{2\tau_{pop}} \frac{\hbar\omega_w^{-\frac{1}{2}}}{kT_L} \frac{d}{dw} \left[\frac{(2n_0 + 1)\hbar\omega_l}{2kT_L} \right]$
	$\ln \frac{4w}{\hbar\omega_l / kT_L} \frac{df_0}{dw} + \ln \frac{4w}{\hbar\omega_l / kT_L} f_0]$	$\ln \frac{4w}{\hbar\omega_l / kT_L} \frac{df_0}{dw} + \ln \frac{4w}{\hbar\omega_l / kT_L} f_0]$
Intervalley optical phonon scattering ^b	$\tau_{intm}^{-1} = \frac{eE_0}{(2m^*kT_L)^{1/2}} (2n_0 + 1)$	$\left \frac{\partial f_0}{\partial \tau} \right = \frac{1}{\tau_{pop}} = \frac{2eE_0}{(2m^*kT_L)^{1/2}}$
	$w^{-\frac{1}{2}}$	$\left \frac{\partial f_0}{\partial \tau} \right = \frac{1}{\tau_{intm}} w^{-\frac{1}{2}} \left[f_0 + w \frac{df_0}{dw} + \frac{2n_1 + 1}{2} \frac{\hbar\omega_l}{kT_L} \frac{df_0}{dw} \right. \\ \left. + w \frac{d^2f_0}{dw^2} \right]$
		$\tau_{intm}^{-1} = \frac{(2m^*)^{\frac{3}{2}} D_i^2 (kT_L)^{\frac{1}{2}}}{4\pi\hbar^3 \rho w_0} (2n_1 + 1)$
		$\frac{1}{\tau_{intm}} = \frac{D_i^2 m^{\frac{3}{2}} (kT_L)^{-\frac{1}{2}}}{\sqrt{2\pi\rho\hbar^2}}$

^aFor details, see ref. [8].^b n_0 and n_1 indicate the equilibrium numbers of phonons for the scatterings.

simultaneously in most semiconductors. The collision term ($df/dt|_{\text{collision}}$) for mixed scattering is a linear combination of the terms for the individual collision processes. The Boltzmann equation for mixed scattering may be written as

$$\frac{2}{3} \frac{eF}{\hbar} E^{-\frac{1}{2}} \frac{d}{dE} \left(E^{\frac{3}{2}} f_1 \right) = \sum_{i=1}^n \frac{\partial f_i}{\partial t} \Big|_{\text{collision},i} \quad (5.6)$$

$$\frac{eF\hbar}{m} \frac{df_0}{dE} = \sum_{i=1}^n \frac{\partial f_i}{\partial t} \Big|_{\text{collision},i} \quad (5.7)$$

With the collision integrals and relaxation times listed in Table 5.1, Eqs.(5.6) and (5.7) can be solved to give the distribution function of electrons as a function of the energy.

5.3 Impact Ionization Coefficients

At very high electric fields, the electrons traveling along the fields can gain enough energy to cause impact ionization as a result of the energy gained from the field in spite of phonon scattering. This impact ionization collision, yielding a new electron-hole pair, could be treated as an additional scattering source to phonon scatterings. Impact ionization is usually known to occur at energies above the ionization threshold energy E_i , which is a characteristic material property. At very high fields, the ionization threshold could be field-dependent. However, it is very difficult to derive a generalized energy

dependency for pair production. Thus, a simple expression developed by Keldysh⁷¹ is frequently used for the frequency of ionizing collisions:

$$\tau_{ii}(E)^{-1} = \tau_s(E_i)^{-1} P \left(\frac{E - E_i}{E_i} \right)^2, \quad E > E_i \quad (5.8)$$

where $\tau_s(E)^{-1}$ = sum of $\tau_i(E_i)^{-1}$ for all the scatterings involved, and P is a dimensionless constant originally assumed by Keldysh to have a value greater than unity. This formula is valid for semiconductors with large dielectric constants and at energies near the ionization threshold. The value of P has usually been taken as a fitting parameter in all the studies reported previously. Interestingly, the values that give the best fit to experimental data have been found to spread over a wide range.

Various scatterings can occur in semiconductors in high electric fields. These include acoustic phonon scattering, nonpolar optical and polar optical phonon scattering, impact ionization scattering, and intervalley phonon scattering. In almost all previous studies, only acoustic and nonpolar optical phonon scatterings have been considered. While nonpolar optical phonon scattering is dominant in nonpolar semiconductors such as Ge and Si, polar optical phonon scattering must also be taken into account in polar semiconductors such as GaAs. Intervalley phonon scattering has also been known to be important for high field transport in both nonpolar⁷⁵ and polar semiconductors⁷⁶.

A. Nonpolar Semiconductors : Si and Ge

The contribution of intervalley scattering to the momentum is usually small in Ge. However, it is not small in Si at high fields, thus requiring solution of coupled Boltzmann equations. This difficulty can be circumvented by taking the electric field in the [111] directions.^{73,77} Electrons in the six satellite valleys may then be considered to behave identically with the field in this direction. Under the condition, only one Boltzmann equation is needed to find the distribution function.

When the impact ionization collision is taken as an additional scattering to other phonon scatterings, the resulting equation governing the distribution of electrons can be derived from the Boltzmann transport equation (See Table 5.1) to be

$$\begin{aligned} \frac{d}{dw} \left[w \left(w\alpha + \frac{2n_1+1}{2} \frac{\hbar\omega_1}{kT_L} \beta + \frac{2n_0+1}{2} \frac{\hbar\omega_0}{kT_L} \right) \frac{df_0}{dw} + w(w\alpha + \beta + 1)f_0 \right] \\ = -\frac{2}{3} \frac{(eF)^2}{m} \frac{\tau_{ope}}{kT_L} \frac{d}{dw} \left(\frac{w}{R_T} \frac{df_0}{dw} \right) \end{aligned} \quad (5.9)$$

where

$$\alpha = \frac{\tau_{ope}}{\tau_{ace}}, \quad \beta = \frac{\tau_{ope}}{\tau_{int\,e}}, \quad w = \frac{E}{kT_L} \quad (5.10)$$

$$R_T = \frac{1}{\tau_{acm}} + \frac{1}{\tau_{opm}} + \frac{1}{\tau_{intm}} + \frac{P(w - w_i)^2}{\tau_s(w_i)w^{\frac{1}{2}}w_i^2}$$

Note that Eq.(5.9) can be obtained by simply substituting $df_0/dt|_i$ and $df_1/dt|_i$ expressions into Eqs.(5.6) and (5.7) with the relaxation time approximation for $df_1/dt|_i$ terms as described before. The effective mass m^* is given by the conductivity effective mass for the electric field in the [111] direction for Si and [100] for Ge. The conductivity effective masses can be reduced to a scalar m^* for all valleys in Si or Ge under the condition even though the effective mass are given in the Appendix C. An assumption in writing Eq.(5.9) is that the optical phonon energy is small compared to the carrier energy. In the high field range of interest, the average carrier energy is expected to be high. Note that the term for impact ionization should be dropped in the above equation for energies less than the ionization threshold energy because ionization cannot occur below the threshold. Also note that a term ($df_0/dt|_{\text{impact ionization}}$) has been ignored in deriving the above equation. The rate of change in the symmetric part of the distribution function due to impact ionization is expected to be very small compared to other phonon scatterings (as will be seen later in Fig.(5.7)).

Integrating Eq.(5.9) once and solving the resultant equation leads to the following for f_0 :

$$f_0(w) = \text{const} \exp\left(-\int_0^w \frac{g(w)}{h(w)} dw\right) \quad (5.11)$$

where

$$h(w) = w\alpha + \frac{2n_1 + 1}{2} \frac{\hbar\omega_1}{kT_L} \beta + \frac{2n_0 + 1}{2} \frac{\hbar\omega_0}{kT_L} + \frac{2}{3} \frac{(eF)^2}{m^*} \frac{\tau_{ope}}{kT_L} R_T^{-1} \quad (5.12)$$

$$g(w) = w\alpha + \beta + 1 \quad (5.13)$$

When w is less than w_i , i.e. below the threshold, impact ionization does not occur, and the above equation for small α reduces to

$$f_0(w) = const \exp\left(-(1+\beta)\frac{w}{\gamma} - \frac{\alpha w^2}{2\gamma}\right) \quad (5.14)$$

where

$$\gamma = \frac{2n_1 + 1}{2} \frac{\hbar\omega_1}{kT_L} \beta + \frac{2n_0 + 1}{2} \frac{\hbar\omega_0}{kT_L} + \frac{2}{3} \frac{(eF)^2}{m^*} \frac{\tau_{ope}}{kT_L} \left(\frac{1}{\tau_{acm}} + \frac{1}{\tau_{opm}} + \frac{1}{\tau_{intm}} \right)^{-1} \quad (5.15)$$

B. Polar Semiconductors : GaAs

In general, inclusion of intervalley scattering leads to coupled Boltzmann equations for central and satellite valleys at high fields. However, the distribution function for satellite valleys is known to be very close to that for the central valley⁷⁶ for large values of

the intervalley deformation potential constant, e.g., 1×10^9 eV/cm. Therefore, one single equation for the central valley may be used to approximate the coupled equations, with the intervalley deformation potential constant as a fitting parameter, especially in calculating the impact ionization coefficient. An additional assumption required here is the use of a spherical band instead of an ellipsoid for the satellite valleys.

Polar optical phonon scattering is neither randomising nor elastic. Hence, strictly speaking, a relaxation time approximation cannot be made for the scattering. However, qualitative features of the scattering are often discussed on the basis of a relaxation time that is defined identically to that for nonpolar optical phonon scattering. As shown in Table 5.2, intervalley optical phonon scattering does have a relaxation time almost identical to that for nonpolar optical phonon scattering. The following equation gives the distribution function f_0 for the combined scattering in a central valley:

$$\begin{aligned} & \frac{1}{\tau_{\text{pope}}} \frac{w^{-\frac{1}{2}}}{kT_L} \frac{d}{dw} \left[\left(\frac{(2n_l + 1)(\hbar\omega_l)^2}{2kT_L} \ln \frac{4w}{\hbar\omega_l / kT_L} + 2kT_L w^2 \alpha_l + \frac{2n_l + 1}{2} w \hbar\omega_l \beta_l \right) \frac{df_0}{dw} \right. \\ & \quad \left. + (\hbar\omega_l \ln \frac{4w}{\hbar\omega_l / kT_L} + 2kT_L w^2 \alpha_l + 2kT_L w \beta_l) f_0 \right] \\ & = -\frac{2(eF)^2}{3m^*} \frac{w^{-\frac{1}{2}}}{kT_L} \frac{d}{dw} \left(\frac{w^{\frac{3}{2}}}{R_T} \frac{df_0}{dw} \right) \end{aligned} \quad (5.16)$$

where

$$\alpha_1 = \frac{\tau_{pope}}{\tau_{ace}}, \quad \beta = \frac{\tau_{pope}}{\tau_{int e}},$$

$$R_T = \frac{\frac{1}{w^2}}{\tau_{acm}} + \frac{\frac{1}{w^2}}{\tau_{int m}} + \frac{\frac{1}{w^2}}{\tau_{popm}} + \frac{P(w - w_i)^2}{\tau_s(w_i)w_i^2}$$
(5.17)

The above equation leads to a solution of f_0 similar to Eq.(5.11). Similar procedures as for Eq.(5.9) have been used for Eq.(5.16).

The electron distribution function obtained here is of the following form:

$$f_0(w) = f_0(w_i) \exp\left(-\int_{w_i}^w \frac{g(w)}{h(w)} dw\right)$$

The difference, when compared to Nag's result⁷³, lies in the expression $h(w)$. In Nag's work, $h(w)$ is linear in w ; in this work, it is nonlinear with the inclusion of impact ionization scattering. As a result, the limits of integration go from w_i to w ; they are from 0 to w in Nag's work. The distribution function is given here for both polar and nonpolar semiconductors; the function is given only for nonpolar semiconductors in Nag's work.

Once the distribution function of electrons is determined, the ionization coefficient α_1 can be calculated easily. Following the usual definition, the impact ionization coefficient is given as the ratio of the average probability of impact ionization to the average electron drift velocity:

Table 5.2. Parameters used for calculations.

<u>Names</u>	<u>Notations</u>	<u>Si</u>	<u>Ge</u>	<u>GaAs</u>
electrons	m_t^*/m_0	0.98	1.64	0.067
	m_t^*/m_0	0.19	0.082	
Effective masses				
holes	m_{th}^*/m_0	0.16	0.044	0.082
	m_{hh}^*/m_0	0.49	0.28	0.45
Equivalent temperature of optical phonon (K)	$\theta_0 (= \hbar\omega_0 / k)$	737	430	417 ^a
Equivalent temperature of intervalley phonon (K)	$\theta_1 (= \hbar\omega_1 / k)$	670	430	334
Average acoustic velocity (cm/s)	C_l	9×10^5	5.32×10^5	5.22×10^5
Density (g/cm ³)	ρ	2.33	5.32	5.31
Drift velocity (cm/s): electrons	v_d	1×10^7	6×10^6	7×10^6
holes	v_d	1×10^7	6×10^6	1×10^7
Ionization threshold energy (eV)	$E_{i,n}$	1.4	0.9	1.6
	$E_{i,p}$	1.7	1.3	2.7
Effective field strength for polar phonon (V/cm)	E_0	5.95×10^3

Table 5.2 continued.

Acoustic phonon deformation				
potential (eV)	E_1	7	9.5	6
Optical phonon deformation	$D_{o,n}$	9×10^8	3.5×10^9	...
potential constant (eV/cm)	$D_{o,p}$	9×10^8	2.0×10^9	...
Intervalley phonon deformation	$D_{l,n}$	2.2×10^9	1.5×10^9	1.38×10^9
potential constant (eV/cm)	$D_{l,p}$	1.7×10^8	1.5×10^9	1.56×10^9
Dimensionless parameter for ionization rate	P_n	0.0012	0.0001	0.0005
	P_p	0.001	0.0008	0.008

^a ω_0 should be interpreted as ω_l .

$$\alpha_i = \frac{\int_{E_i}^{\infty} \tau_u(E)^{-1} \Omega(E) f_0(E) dE}{v_d \int_0^{\infty} \Omega(E) f_0(E) dE} \quad (5.18)$$

where $\Omega(E)$ is the density of states and v_d is the electron drift velocity. Although non-parabolic band structure was used in recent studies^{72,77}, simple parabolic band structure was used here for the density of states. More detailed band structures such as those due to Kane⁷⁸ for GaAs and those due to Cardona and Pollak⁴¹ for Si and Ge could have been used for the density of states. The results presented here, however, would not have changed except for changes in the fitting parameters, which would be in the range of the uncertainties of parameters.

5.4 Comparison and Discussion

The theoretical results obtained for the energy distribution and impact ionization coefficients do not involve any adjustable parameters in principle, since the expressions contain only physical constants and parameters whose values are rather well established. There are two exceptions, however, namely the optical phonon deformation potential (D_0) and/or the intervalley phonon deformation potential (D_1), and the parameter P in expression (5.8) for the frequency of impact ionization.

Knowledge of the deformation potential is very limited although some theoretical and experimental estimates have been made. Different studies give different values of the potential. For electrons in *n*-type Si, the nonpolar optical phonon deformation potential

constant ranges from 1.5×10^8 to 1×10^9 eV/cm⁷⁹⁻⁸¹ while it ranges from 6×10^8 to 7×10^8 for *p*-type Si for the valence band edge at the Γ point. Germanium⁸² has larger values, about 1.15×10^9 eV/cm. There are other likely probabilities with which the equivalent or nonequivalent intervalley scatterings (*L-L*, *X-L*, Γ -*L*, etc.) occur. Very few deformation potential constants have been reported for intervalley scattering^{75,79}. For simplicity, *X-L* intervalley for Si and *L-L* intervalley scattering for Ge were picked. In the case of GaAs, polar optical phonon scattering must be taken into consideration in place of nonpolar scattering. For the intervalley scattering here, the Γ -*L* intervalley scattering was used. Because there are more uncertainties in the deformation potential constant for intervalley scattering, this potential was chosen as a fitting parameter.

A few comments are in order here for the value of 2.2×10^9 chosen for the intervalley phonon deformation potential, which is about 100 % higher than the values typically used⁷⁹. Although the uncertainties regarding the values of nonpolar optical and intervalley phonon deformation potential constants could be a contributing factor, approximation of coupled Boltzmann equations with a single equation for the central valley could have resulted in the high value. It is noted in this regard that use of a higher value of nonpolar optical phonon deformation potential constant results in a lower value of the intervalley phonon deformation potential constant.

The impact ionization threshold energies used here are those due to Monch⁸³. Extensive theoretical studies^{83,84} have shown that the values of the threshold energies can vary depending on the theory but that the difference does not result in a large discrepancy in the calculated impact ionization coefficient.

Since the introduction of the simple expression for ionization rate Eq.(5.8) by Keldysh, many values of P differing by orders of magnitude have been reported. Chwang, Kao, and Crowell⁸⁵ used values of P much larger than unity, even assuming a value of infinity of their calculation. Baraff⁶⁸ concluded that the impact ionization rate does not depend on this parameter strongly, provided its value is large compared to unity. Shichijo and Hess⁸⁶ varied P between 50 and 400 in their Monte Carlo simulation. On the other hand, the value of P would be of the order of 10^{-3} if their results from the scattering rate for pair production in Si (Ref.87) was interpreted according to Keldysh's formula. According to Tang and Hess⁷⁵, the hot electron emission from Si to SiO_2 could only be explained if P was about 10^2 . Ridley⁷⁰ obtained an explicit expression for the ionization rate near the threshold assuming spherical parabolic bands, yielding a value of 0.005 for GaAs. Marsland⁸⁸ also showed that very small values of P fitted experimental data very well. The values of P I have chosen for calculations are given in Table 5.3 along with Ridley's⁷⁰ and Marsland's⁸⁸.

The experimental results reported in the literature from nine different sources have been fitted by selecting the values of D_1 (intervalley deformation potential) and P . Note that the same set of D_1 and P values are applicable to all the experimental results. The values of physical constants and parameters including those of D_1 and P are given in Table 5.2. It is noted in this regard that the deformation potential constant affects mainly the slopes of the curves of the impact ionization coefficient, α_i , vs. $1/F$ where F is the field; the parameter P only moves the whole curve up or down on the α_i axis. Because of the

Table 5.3. Comparison of this results with those of Marsland (Ref. 88) and Ridley (Ref. 70).

		E_i	P		
			This work	Marsland	Ridley
Si :	electrons	1.4	1.1	1.2	0.0012
	holes	1.7	1.8	1.8	0.001 0.0032
GaAs :	electrons	1.6	1.7	1.7	0.0005 0.0068
	holes	2.7	1.424	1.6	0.008 0.0037 0.0067

two distinctly different effects of the two parameters, there can exist only one set of parameter values giving the best fit to all the experimental data compared here.

Shown in Fig.5.1 is a comparison between calculated and experimental values⁸⁹⁻⁹¹ for Si for both electrons and holes. The solid lines represent the prediction of the model. Fig.5.2 shows a similar comparison for electrons in Ge;^{92,93} Fig.5.3 is for holes in Ge. The impact ionization coefficient for electrons in GaAs is compared with experimental data⁹⁴⁻⁹⁶ in Fig.5.4 and that for holes in GaAs in Fig.5.5. The temperature dependence of the ionization coefficients is shown in Fig.5.6 for the data at 213 K and 100 K when the parameter values at 300 K are used as the basis. The comparisons given in Figs.5.1 through 5.6 show good agreement with experimental results.

A large value of P , which is a measure of hardness of the threshold, means a higher ionization rate. To assess the effect of impact ionization, the energy distribution function of electrons was calculated for Si as a function of the field both with (solid lines) and without (dashed lines) impact ionization scattering. As shown in Fig. 5.7, the impact ionization disturbs the electron energy distribution little above the threshold energy of 1.4 eV for Si. In the case of GaAs, the contribution of impact ionization to the electron energy distribution is even smaller and hardly noticeable.

Figure 5.8 shows the individual components of all scattering rates considered for GaAs. It is seen that intervalley optical phonon scattering is dominant over the entire range of electron energy and its scattering time exceeds 10^{-14} s, in agreement with the result of Hess *et al.*⁹⁷

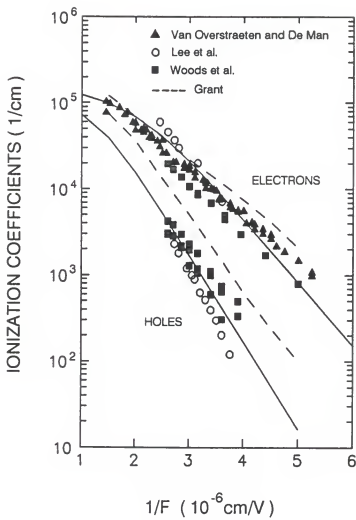


Fig. 5.1. Ionization coefficient of holes and electrons in Si. The solid line represents the theoretical prediction.

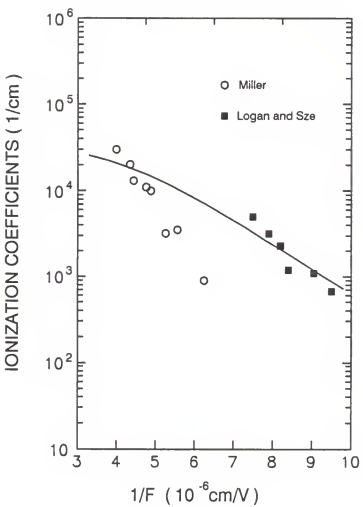


Fig.5.2. Ionization coefficient of electrons in Ge.

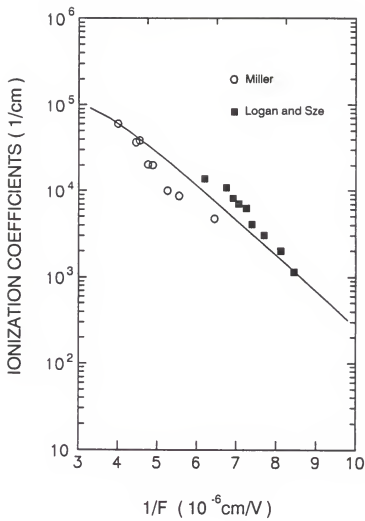


Fig.5.3. Ionization coefficient of holes in Ge.

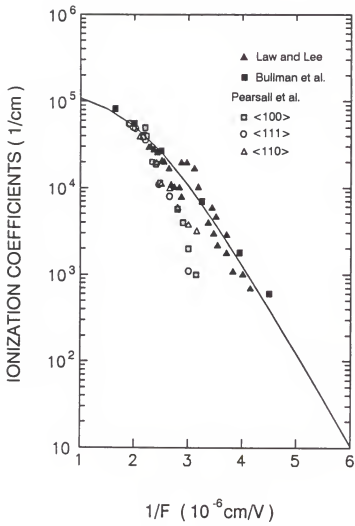


Fig. 5.4. Ionization coefficient of electrons in GaAs.

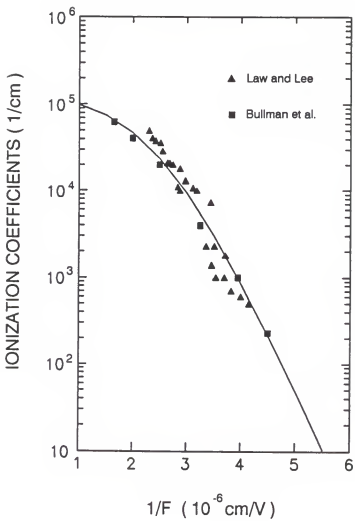


Fig.5.5. Ionization coefficient of holes in GaAs.

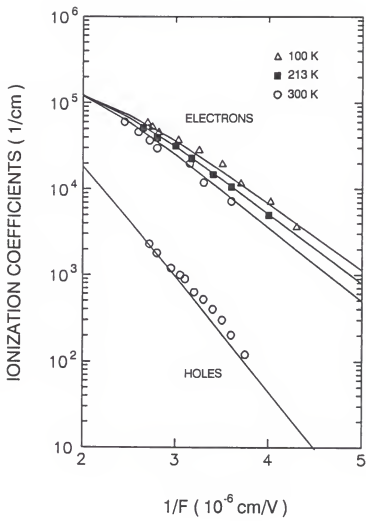


Fig.5.6. Temperature dependence of ionization coefficient (silicon).

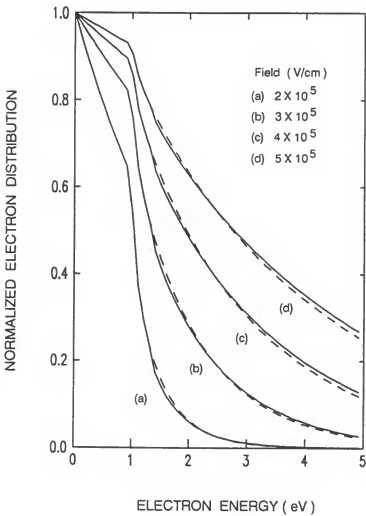


Fig. 5.7. Electron energy distribution function for silicon as a function of field with (solid line) and without (dashed line) impact ionization.

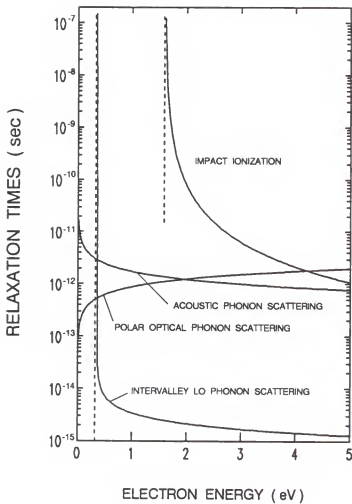


Fig. 5.8. Individual relaxation times of electrons in GaAs.

5.5 Conclusion

An approximate solution of the Boltzmann transport equation is used to arrive at an expression for the electron energy distribution function. All major scattering mechanisms, including intervalley scattering, are included, and a distinction is made between nonpolar (Si, Ge) and polar (GaAs) optical phonon scattering. Numerically calculated impact ionization coefficients for electrons and holes in Ge, Si, and GaAs compare favorably with almost all experimental results reported in the literature. In polar semiconductors, in particular GaAs, intervalley scattering is found to dominate.

CHAPTER 6

VOLTAGE TUNABLE INFRARED DETECTORS

6.1 Introduction

Most of the semiconductor devices are made by doped *p-n* junctions and/or heterostructures. For all those junctions, there is one thing in common; that is, they connect two semiconductor layers with different bands. The bands of a *p-n* junction are controlled by the dopants, while the bands of a heterojunction are changed by the alloy compositions.

The superlattice is made of periodic junctions such that the bands connected by the junctions form a one-dimensional periodic potential. Because of this one-dimensional potential superimposed on the real crystal potential, minibands are formed within the conduction and valence bands. In general, a superlattice is composed of a period of a simple element, *e.g.*, square shape or a triangle potential. The building block of the superlattice, however, can also be any arbitrary potential well. In addition, many different superlattices can be put together to form a device structure. Specially, this kind of device structure used to be referred to a multiple superlattice. The junctions between the multiple superlattices can be divided into two categories which are band alignment and band stop. The division depends upon whether the miniband on either side of the junction is aligned to the other or not. This new multiple superlattice using the aligned minibands is referred to band aligned superlattice (BAS).⁹⁹

Using the concept of the BAS, voltage tunable infrared detector could be realized. For an example, Grave *et al.* recently reported that their GaAs/Al_xGe_{1-x}As multistack quantum well infrared detector showed a wide spectral response and a tunable voltage-controlled multispectral response.³³ The intersubband infrared detector consists of three stacks of quantum wells, of which energy subbands are aligned. The quantum wells in a given stack are identical, but are different from stack to stack. Each stack is designed to yield an absorption and a photoresponse at a different peak wavelength. This detector functions as a bound-to-continuum infrared detector.²¹

Conventionally, for voltage tunable detector, the quantum-confined Stark effect has been of greater interest, which describes the effect of applied electric fields on the energy levels in quantum wells.^{21,30,31} As mentioned earlier in chapter 1, the quantum-confined Stark effect is more pronounced when a stepped well structure is used. It has been shown in stepped quantum well superlattices that highly voltage-tunable infrared detection can be realized by adjusting the energy levels (intersubband) with an applied electric field,^{31,32} in other words, by utilizing the Stark effect. Also, a structure similar to the superlattice has been studied for direct band gap material.⁶³ Although the results have been obtained for GaAs/Al_xGa_{1-x}As, the same phenomena should be applicable to Si/Si_{1-x}Ge_x, the idea being that the flexibility afforded should enhance the tunability for different wavelengths when applied to the superlattice.

In this chapter, both band aligned superlattice and stepped well superlattice are discussed for an application for voltage tunable infrared detector. For the theoretical bases, the band structures of superlattices of variable basis, the intersubband optical

transitions, and the effect of applied electric field on the superlattices has already been studied through chapter 2 to 4.

6.2 Band Aligned Superlattice

The simple band aligned structure shown in Fig. 6.1 is composed of three superlattices (SL1, SL2, and SL3). The ground miniband in SL1 is aligned with that in SL2 and SL3. The highest miniband in SL3 is aligned with that in SL1 and SL2, so that the transport in the highest band can occur continuously at the superlattice junctions. Likewise, the second highest miniband in SL2 is aligned with that in SL3. As shown in Fig. 6.1, this BAS structure is incorporated with a resonant-tunnelling collector. The SL1 is composed of 12 monolayers of Si well and $\text{Si}_{0.5}\text{Ge}_{0.5}$ barriers. The SL2, which is a two-well coupled superlattice, has a period that forms 12 monolayers of Si well and 10 monolayers of $\text{Si}_{0.5}\text{Ge}_{0.5}$ barrier followed by 15 monolayers of the well and 10 monolayers of the same barrier. The last part of the BAS, SL3 consists of 10 monolayers of Si well and 30 monolayers of $\text{Si}_{0.75}\text{Ge}_{0.25}$ middle barrier followed by 15 monolayers of $\text{Si}_{0.5}\text{Ge}_{0.5}$ barrier.

The energy band structures of the three different superlattices are shown in Fig. 6.2, which are calculated by the method described in chapter 2. The energy minibands of the superlattices are aligned each other such a way of the alignments which are roughly shown in Fig. 6.1. In SL1, optical transition should occur at transition wavelength of about $6.2 \mu\text{m}$, which approximately corresponds to transition energy of 200 meV. On the other hand, the approximate wavelengths of the dominant intersubband transition in SL2

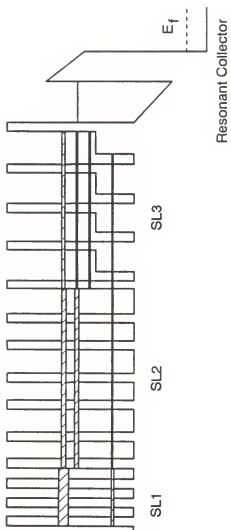


Fig. 6.1. Band aligned superlattice with a resonant collector

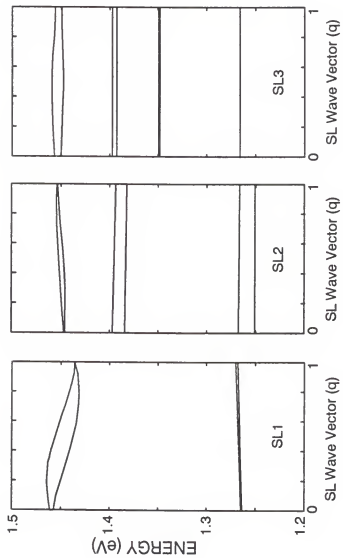


Fig. 6.2. Energy band structures of the three superlattices.

and SL3 are 8.3 and 15 μm , respectively. Here, the dominant transition indicates a transition at the longest peak wavelength, which should have the highest oscillator strength among all the possible transitions. The electrons populating in the upper miniband in SL1, due to optical transition, are transmitted through the aligned minibands in SL2 and SL3 by miniband conduction. The second highest minibands in SL2 and SL3 should have high electron density after intersubband transitions in SL2 and subsequent transmission through the aligned band occur. Likewise, the second lowest miniband in SL3 is also populated by electrons due to transitions therein.

The transmission coefficient of each superlattice is shown in Fig. 6.3. The peaks of the transmission coefficient are proven located around the miniband energies of the superlattices. The transmission coefficient can be obtained by using the envelope function approximation (EFA), which has been explained in chapter 2. The calculation procedure is relatively simple and could be found in the literature,⁶³ where used a single wave function approximation instead of the complete multicomponent envelope functions. The complete envelope functions are used in this study for calculations of the transmission coefficient. However, the calculation procedure is almost identical to the approximate calculation in principle, so it is not explained here in order to avoid redundancy. Because of high transmission coefficients at the miniband energies, the photo-excited electrons move rather freely through the aligned minibands.

By incorporating a resonant-tunneling collector in the right side of the BAS, photocurrent induced by the optical transitions in each superlattice can flow out to be detected with the photocurrent measurement. The resonant collector should be designed

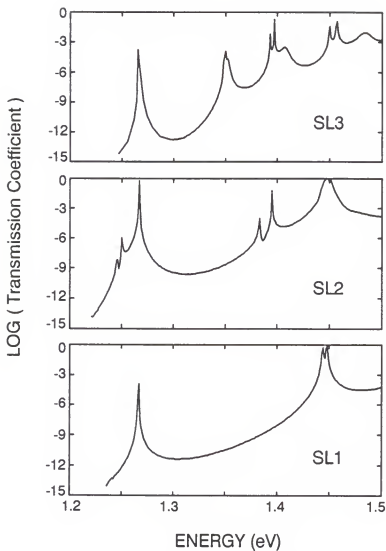


Fig. 6.3. The transmission coefficient for the three superlattices.

to allow only one bound energy level, which could be adjusted to be aligned with different miniband energies by changing the applied electric field. In order to have all the voltage drop in the undoped resonant collector part only, the superlattices are *n*-type doped and both contact are assumed to be *n*-type. To describe the working principle of the resonant collector BAS, the voltage drop is inevitably assumed to be sustained only by the intrinsic region, i.e., the resonant collector. For more detailed analysis, a self-consistent calculation with the Poisson equation should be incorporated.

When a low electric field is applied, an energy level in the resonant collector could be aligned with the highest aligned miniband in the BAS to collect electrons that are photo-excited mainly in SL1 and transported to the junction between SL3 and the collector. With higher electric fields applied, the energy level in the collector should be lowered. As soon as the energy level in the collector becomes aligned again with other lower minibands, electrons in the aligned miniband can tunnel through the collector. Thus, by changing the electric field, the photocurrent could be measured at three different wavelengths of 6.2, 8.3, and 15 μm .

There are several nonideal factors which might cause problems of miniband alignment. First of all, the well width variations may cause a shift of miniband energies. For example, one monolayer change in a well may cause energy shifts and result in misalignment of the minibands. To minimize the band misalignment caused by well width variation, thinner barriers are desirable so that the wells are strongly coupled and the minibands can overlap appreciably.

Second, the flat band condition shown in Fig. 6.1 could not be realistic when there is a band bending caused by doping and free carrier distribution. However, the miniband misalignment caused by band bending can be overcome by modulation doping. The doping density required for flat band condition can be estimated such a way that the doping in each superlattice should be equal to the corresponding free carrier concentration.

6.3 Stepped Well Superlattice

A stepped well superlattice is shown in Fig.6.4. It has been known that a stepped well structure exhibits greater voltage tunability of intersubband transition wavelengths because of the fact that the energy levels can be bounded in different section of a well. As shown in Fig.6.4, the lower level is bounded in narrower well while the upper level is in wider well. Since the Stark energy shift due to electric field strongly depends on width of a well, the two energy levels shift in different amounts when the applied electric field changes. Thus, it results in the voltage tunability of the absorption wavelengths. After the intersubband transition occurs, the photo-excited electrons in the upper band easily tunnel out of the wells as shown in Fig. 6.4, thereby producing a photocurrent. As mentioned earlier in chapter 4, higher probability of interwell transitions is expected than that of intrawell transitions at low electric fields. In order to prevent the interwell transition from occurring, it is desirable to use thick barriers.

By using the stepped well superlattice, switchable wavelength infrared detector¹⁰⁰ is another possibility. While the stepped well superlattice described above only exploits

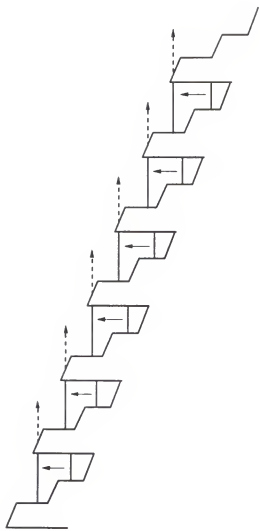


Fig. 6.4. A stepped well superlattice under an electric field.

bound to bound transition, this switchable infrared detector uses both bound to bond and bound to continuum transitions. This structure is shown in Fig. 6.5. At a low electric field, both bound to bound and bound to continuum transitions can occur, of which the bound to bound transition is dominant in strength. However, since the tunnelling probability of photoexcited electrons in the upper bound state should be very low due to thick barrier width, only the bound to continuum transition results in a photocurrent, as shown in Fig. 6.5 (b). Therefore, only a shorter absorption wavelength of the two possible wavelengths is expected to be detected by the measurement. When a high electric field is applied, the barrier width becomes considerably narrower and it allows for electrons to tunnel out easily as shown in Fig. 6.5 (a). In this case both transitions may contribute to the photocurrent and the contribution of each transition depends on the applied electric field. Obviously, as higher electric field is applied, the more dominant the bound to bound transition becomes. Thus, this structure can switch two different wavelengths by changing the applied electric field.

6.4 Concluding Remarks

It is true that voltage tunable infrared detector using the $\text{Si}/\text{Si}_{1-x}\text{Ge}_x$ superlattice should be realized if the detector is possible to be made by $\text{GaAs}/\text{Al}_x\text{Ga}_{1-x}\text{As}$ structures. In most cases, the $\text{GaAs}/\text{Al}_x\text{Ga}_{1-x}\text{As}$ heterostructures has been the first choice in materials for optical device applications. And many experimental evidences have been given for realization of the optical devices. In recent years, however, the studies of the $\text{Si}/\text{Si}_{1-x}\text{Ge}_x$ superlattice for the applications have become popular, but still very little experimental

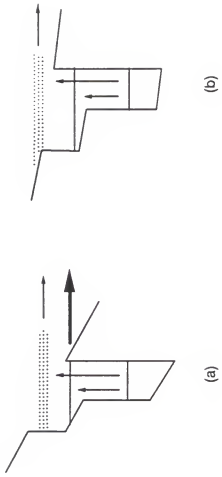


Fig. 6.5. A stepped well structure under different electric fields; (a) high electric field,
(b) low electric field.

efforts have been devoted. The structures for voltage tunable detector presented here should be considered as possible concepts since no experimental evidences have been available. Nevertheless, it should be also true that there would be a lot more novel structures to be devised in the near future, utilizing the advantages of this superlattice .

APPENDIX A
THE $\mathbf{k} \cdot \mathbf{p}$ HAMILTONIAN FOR Ge AND Si IN THE [100] DIRECTION

Theoretically an infinite number of plane waves is required for describing energy bands for the "empty" crystal lattices. It is a well-known fact that the real energy bands for a material are obtained by a small perturbation of the empty lattice bands. In 1966 Cardona and Pollak³⁹ found that there should be a large energy gap between the [200] and [220] plane waves. This led them to suggest the possibility of a $\mathbf{k} \cdot \mathbf{p}$ description of the energy bands of Ge and Si using as a basis only the 15 states of the real crystal which correspond to [000], [111], and [200] plane wave states in the empty lattice. This set of plane waves contains Γ_1 twice, Γ_2 twice, Γ_{25} twice, $\Gamma_{12'}$ once, and Γ_{15} once, as shown in Fig. A1.

The nomenclature for the wave functions is as follows: Γ_2' and Γ_2'' are denoted by S and S' respectively, which transform like xyz; Γ_{25} contains X, Y, and Z transforming like yz, zx, and xy, with Γ_{25}' and Γ_{25}'' ; Γ_{15} contains x, y, and z; $\Gamma_{12'}$ contains γ_1 and γ_2 . All the functions are chosen real except γ_1 and γ_2 which are arranged in pure imaginary combinations. The nomenclatures and wave functions are summarized in the following table.

It should be noted here that the $\Gamma_{12'}$ wave functions are taken to have the symmetry of $\sqrt{3}(y^2 - z^2)(\Gamma_{12'}^{(1)})$ and $(3x^2 - r^2)(\Gamma_{12'}^{(2)})$, where $\Gamma_{12'}^{(1)}$ and $\Gamma_{12'}^{(2)}$ satisfy the relationships of $\Gamma_{12'}^{(1)} = (1/\sqrt{2})(\gamma_1 - \gamma_2)$ and $\Gamma_{12'}^{(2)} = (1/\sqrt{2})(\gamma_1 + \gamma_2)$.

By using the proper selection rules, it can be seen that the $\mathbf{k} \cdot \mathbf{p}$ Hamiltonian is determined by 10 matrix elements of \mathbf{p} . The matrix elements are given elsewhere.^{5,63} The final Hamiltonian is shown in the following tables for the [100] growth directions. For the [111] and [110] directions, proper transformations are needed to result in simpler block-diagonalized matrices.

The general Hamiltonian matrix without spin is given in Table A2 and the matrix in the [100] direction is given in Table A3. The Hamiltonian matrix can be block-diagonalized into three independent matrices. The matrices in [100] direction are given in Table A4.

Table A1. Irreducible representations and basis functions.

<u>Irreducible Representation</u>	<u>state (k=0)</u>	<u>plane-wave and atomic state</u>	<u>Basis functions</u>
Γ_{25}'		[111], p+	xy, yz, zx
Γ_2'		[111], s-	xyz
Γ_{15}		[111], p-	x, y, z
Γ_1''		[111], s+	constant
Γ_1'		[000], s+	constant
Γ_{12}'		[200], d-	$\sqrt{3}xyz(y^2 - z^2), xyz(3x^2 - r^2)$
Γ_{25}''		[200], d+	xy, yz, zx
Γ_2''		[200], s-	xyz

energy in eV

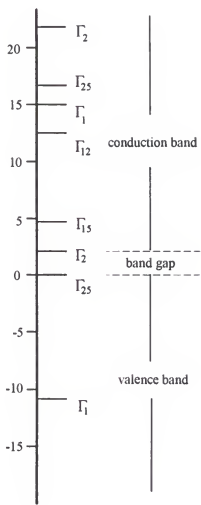


Fig.A1. The order of the energy levels at $k=0$ in Ge.

Table A2. The $\mathbf{k} \cdot \mathbf{p}$ Hamiltonian Matrix without Spin.

Γ_{1x}^r	Γ_{2x}^r	Γ_{3x}^r	Γ_{1z}^r	Γ_{15}^r	Γ_{15}^r	Γ_i^r	Γ_i^r	Γ_{12}^{r0}	Γ_{12}^{r0}	Γ_{2x}^r	Γ_{3x}^r
k^2			Pk_z	Pk_z	Qk_z	Qk_z	Qk_z	$\sqrt{2Rk_z}$	$\sqrt{2Rk_z}$	P^*k_z	P^*k_z
Γ_{1x}^r	k^2		Pk_z	Qk_z	Qk_z	Qk_z	Qk_z	$-\sqrt{1/2Rk_z}$	$-\sqrt{1/2Rk_z}$	P^*k_z	P^*k_z
Γ_{2x}^r	Pk_z	$\sqrt{3/2Rk_z}$	$-\sqrt{3/2Rk_z}$	Q^*k_z	Q^*k_z						
Γ_{1z}^r	Qk_z	$\sqrt{3/2Rk_z}$	$-\sqrt{3/2Rk_z}$	Q^*k_z	Q^*k_z						
Γ_{15}^r	Qk_z	$\sqrt{3/2Rk_z}$	$-\sqrt{3/2Rk_z}$	Q^*k_z	Q^*k_z						
Γ_i^r	Qk_z	$\sqrt{3/2Rk_z}$	$-\sqrt{3/2Rk_z}$	Q^*k_z	Q^*k_z						
Γ_1^r	Tk_z	$\sqrt{3/2Rk_z}$	$-\sqrt{3/2Rk_z}$	P^*k_z	P^*k_z						
Γ_1^r	Tk_z	$\sqrt{3/2Rk_z}$	$-\sqrt{3/2Rk_z}$	P^*k_z	P^*k_z						
Γ_1^r	Tk_z	$\sqrt{3/2Rk_z}$	$-\sqrt{3/2Rk_z}$	P^*k_z	P^*k_z						
Γ_{12}^{r0}	$\sqrt{3/2Rk_z}$	$\sqrt{3/2Rk_z}$	P^*k_z	P^*k_z							
Γ_{12}^{r0}	$\sqrt{3/2Rk_z}$	$\sqrt{3/2Rk_z}$	P^*k_z	P^*k_z							
Γ_{2x}^r	P^*k_z	$\sqrt{3/2Rk_z}$	$-\sqrt{3/2Rk_z}$	P^*k_z	P^*k_z						
Γ_{3x}^r	P^*k_z	$\sqrt{3/2Rk_z}$	$-\sqrt{3/2Rk_z}$	P^*k_z	P^*k_z						

Table A3. Hamiltonian in the [100] direction.

Table A4. Block-diagonalized matrices in the [100] direction.

(a). Δ_1 band, including the lowest conduction band in silicon;

$$\begin{vmatrix} \Gamma_{15} + k_x^2 & Tk_x & T'k_x \\ Tk_x & \Gamma_1'' + k_x^2 & 0 \\ T'k_x & 0 & \Gamma_1' + k_x^2 \end{vmatrix}$$

(b). two doubly degenerate Δ_5 bands;

$$\begin{vmatrix} k_x^2 & Qk_x & 0 \\ Qk_x & \Gamma_{15} + k_x^2 & Q'k_x \\ 0 & Q'k_x & \Gamma_{25}'' + k_x^2 \end{vmatrix}$$

(c). Δ_2 band;

$$\begin{vmatrix} \Gamma_2' + k_x^2 & Pk_x & 0 & P'k_x & 0 \\ Pk_x & k_x^2 & \sqrt{2}Rk_x & 0 & P''k_x \\ 0 & \sqrt{2}Rk_x & \Gamma_{12}'' + k_x^2 & \sqrt{2}R'k_x & 0 \\ P'k_x & 0 & \sqrt{2}R'k_x & \Gamma_{25}'' + k_x^2 & P'''k_x \\ 0 & P''k_x & 0 & P'''k_x & \Gamma_2'' + k_x^2 \end{vmatrix}$$

APPENDIX B
ELEMENTS OF THE TRANSFER MATRIX FOR BULK, M

$$M_{11} = \lambda_1 k_2 C_1 / D_1 - \lambda_2 k_1 C_2 / D_1$$

$$M_{12} = \lambda_1 \lambda_2 k_2 S_1 / D_2 - \lambda_1 \lambda_2 k_1 S_2 / D_2$$

$$M_{13} = \lambda_1 S_1 / D_2 - \lambda_2 S_2 / D_2$$

$$M_{14} = -\lambda_1 \lambda_2 C_1 / D_1 + \lambda_1 \lambda_2 C_2 / D_1$$

$$M_{21} = k_2 S_1 / D_1 - k_1 S_2 / D_1$$

$$M_{22} = -\lambda_2 k_2 C_1 / D_2 + \lambda_1 k_1 C_2 / D_2$$

$$M_{23} = -C_1 / D_2 + C_2 / D_2$$

$$M_{24} = -\lambda_2 S_1 / D_1 + \lambda_1 S_2 / D_1$$

$$M_{31} = \lambda_1 k_1 k_2 S_1 / D_1 + \lambda_2 k_1 k_2 S_2 / D_1$$

$$M_{32} = \lambda_1 \lambda_2 k_1 k_2 C_1 / D_2 - \lambda_1 \lambda_2 k_1 k_2 C_2 / D_2$$

$$M_{33} = \lambda_1 k_1 C_1 / D_2 - \lambda_2 k_2 C_2 / D_2$$

$$M_{34} = \lambda_1 \lambda_2 k_1 S_1 / D_1 - \lambda_1 \lambda_2 k_2 S_2 / D_1$$

$$M_{41} = k_1 k_2 C_1 / D_1 - k_1 k_2 C_2 / D_1$$

$$M_{42} = \lambda_2 k_1 k_2 S_1 / D_2 - \lambda_1 k_1 k_2 S_2 / D_2$$

$$M_{43} = k_1 S_1 / D_2 - k_2 S_2 / D_2$$

$$M_{44} = -\lambda_2 k_1 C_1 / D_1 + \lambda_1 k_2 C_2 / D_1,$$

where

$$C_i = \cos(k_i x)$$

$$S_i = \sin(k_i x)$$

$$D_1 = \lambda_1 k_2 - \lambda_2 k_1$$

$$D_2 = \lambda_1 k_1 - \lambda_2 k_2.$$

APPENDIX C CONDUCTIVITY EFFECTIVE MASS

The conductivity effective masses can be defined by

$$m^* = 3[(1/m_l^*) + (2/m_h^*)]^{-1} \quad (C1)$$

for electrons, and

$$m^* = m_{ch}^* \left[1 + \left(\frac{m_{lh}^*}{m_{hh}^*} \right)^{\frac{3}{2}} \right] \left[1 + \left(\frac{m_{lh}^*}{m_{hh}^*} \right)^{\frac{3}{2}} \frac{m_{ch}^*}{m_{cl}^*} \right]^{-1}$$

for holes, where m_{ch} and m_{cl} are the conductivity effective masses for heavy and light holes, respectively. The m_{ch} and m_{cl} are given by the following equation:⁷³

$$m_{c\mp}^* = m_0 (1 + 0.0333 Y_\mp - 0.0257 Y_\mp^2) / (A \pm B') \quad (C2)$$

and

$$B' = (B^2 + \frac{1}{6} C^2)^{\frac{1}{2}}, \quad (C3)$$

$$Y_\mp = \mp \frac{1}{2} \left[\frac{C^2}{B'(A \pm B')} \right], \quad (C4)$$

where A, B and C are the parabolicity constants for the valence bands of Si and Ge. Here I have chosen the values of A=4.1, B=1.6, and C=3.3 for Si, and A=13.0, B=8.9, and C=10.3 for Ge.⁹⁸

REFERENCES

1. Peterson, K. E., Proc. IEEE **70**, 420 (1982).
2. Esaki, L., and Tsu, R., IBM J. Res. Develop. **40**, 61 (1970).
3. Mukherji, D., and Nag, B. R., Phys. Rev. **B12**, 4338 (1975).
4. de Sterke, C. M., and Hall, D. G., Phys. Rev. **B35**, 1380 (1987).
5. Rajakarunanayake, Y., and McGill, T. C., Phys. Rev. **B40**, 3051 (1989).
6. Lee, H. H., Phys. Rev. **B43**, 14692 (1991).
7. Morrison, I., Jaros, M., and Wong, K. B., Phys. Rev. **B35**, 9693 (1987).
8. Turton, R. J., Jaros, M., and Morrison, I., Phys. Rev. **B38**, 8397 (1988).
9. Turton, R. J., and Jaros, M., Appl. Phys. Lett. **54**, 1986 (1989).
10. Turton, R. J., and Jaros, M., Appl. Phys. Lett. **56**, 767 (1990).
11. Rajakarunanayake, Y., and McGill, T. C., J. Vac. Sci. Technol. **B8**, 929 (1990).
12. Yang, C.-I., and Pan, D.-S., J. Appl. Phys. **64**, 1573 (1998).
13. Yang, C.-I., Pan, D.-S., and Somoano, R., J. Appl. Phys. **65**, 3253 (1989).
14. Rajakarunanayake, Y., and McGill, T. C., Appl. Phys. Lett. **55**, 1537 (1989).
15. Ismail, K., Meyerson, B. S., and Wang, P. J., Appl. Phys. Lett. **58**, 2117 (1991).
16. Mii, Y. J., Xie, Y. H., Fitzgerald, E. A., Monroe, D., Thiel, F. A., Weir, B. E., and Feldman, L. C., Appl. Phys. Lett. **59**, 1661 (1991).
17. Luryi, S., Pearsall, T. P., Tempkin, H., and Bean, J. C., IEEE Electron Device Lett. **EDL-7**, 104 (1986).

18. Pearsall, T. P., Tempkin, H., Bean, J. C., and Luryi, S., IEEE Electron Device Lett. EDL-7, 330 (1986).
19. Levine, B. F., Choi, K. K., Bethea, C. G., Walker, J., and Malik, R. J., Appl. Phys. Lett. 50, 1092 (1987).
20. Choi, K. K., Levine, B. F., Bethea, C. G., Walker, J., and Malik, R. J., Appl. Phys. Lett. 50, 1814 (1987).
21. Levine, B. F., Bethea, C. G., Hasnain, G., Walker, J., and Malik, R. J., Appl. Phys. Lett. 53, 296 (1988).
22. Levine, B. F., Bethea, C. G., Hasnain, G., Shen, V. O., Pelve, E., Abbott, R. R., and Hsieh, S. J., Appl. Phys. Lett. 56, 851 (1989).
23. Kingston, R. H., "Detection of Optical and Infrared Radiation," Springer, New York (1978).
24. Abstreiter, G., Brugger, H., Wolf, T., Jorke, H., and Herzog, H. J., Phys. Rev. Lett. 54, 2442 (1985).
25. Karunasiri, R. P. G., Park, J. S., Wang, K. L., and Cheng, L.-J., Appl. Phys. Lett. 56, 1342 (1990).
26. Karunashiri, R. P. G., Park, J. S., and Wang, K. L., Appl. Phys. Lett. 59, 2588 (1991).
27. Hertle, H., Schuberth, G., Gornik, E., Absteriter, G., and Schaffler, F., Appl. Phys. Lett. 59, 297 (1991).
28. Fujita, K., Fukatsu, S., Shiraki, Y., Yaguchi, H., and Ito, R., Appl. Phys. Lett. 61, 210 (1992).
29. Chang, Y.-C., Chiou, A. E., and Khoshnevisan, M., J. Appl. Phys. 71, 1349 (1992).
30. Choi, K. K., Levine, B. F., Bethea, C. G., Walker, J., and Malik, R. J., Phys. Rev. B 39, 8029 (1989).
31. Parihar, S. R., Lyon, S. A., Santos, K., and Shayegan, M., Appl. Phys. Lett. 55, 2417 (1989).
32. Karunasiri, R. P. G., Mii, Y. J., and Wang, K. L., IEEE Elect. Dev. Lett. 11,

227 (1990).

33. Grave, I., Shakouri, A., Kuze, N., and Yariv, A., Appl. Phys. Lett. **60**, 2362 (1992)
34. Capasso, F., Tsang, W. T., Hutchinson, A. L., and Williams, G. F., Appl. Phys. Lett. **40**, 38 (1982).
35. Hull, R., Gibson, J. M., and Bean, J. C., Appl. Phys. Lett. **46**, 179 (1985).
36. Moriarti, J. A., and Krishnamurti, S., J. Appl. Phys. **54**, 1892 (1983).
37. Krishnamurti, S., and Moriarti, J. A., Phys. Rev. B **32**, 1027 (1985).
38. Bastard, G., Phys. Rev. B **24**, 5693 (1981).
39. Bastard, G., Phys. Rev. B **25**, 7584 (1982).
40. Luttinger, J. M., and Kohn, W., Phys. Rev. **97**, 869 (1955).
41. Cardona, M., and Pollak, F. H., Phys. Rev. **142**, 530 (1966).
42. Van de Walle, C. G., and Martin, R. M., Phys. Rev. B **34**, 5621 (1986).
43. People, R., IEEE J. Quantum Electron. QE-22, 1696 (1986).
44. Balslev, I., Phys. Rev. **143**, 636 (1966).
45. Ahn, D., and Chuang, S. L., Phys. Rev. B **35**, 4149 (1987).
46. Ahn, D., and Chuang, S. L., IEEE J. Quantum Electron. QE-23, 2196 (1987).
47. Austin, E. J., and Jaros, M., Appl. Phys. Lett. **47**, 274 (1985).
48. Austin, E. J., and Jaros, M., J. Appl. Phys. **62**, 558 (1987).
49. McIlroy, P. W. A., J. Appl. Phys. **59**, 3532 (1986).
50. Hagon, J. P., and Jaros, M., Phys. Rev. B **41**, 2900 (1990).
51. Bastard, G., Mendez, E. E., Chang, L. L., and Esaki, L., Phys. Rev. B **28**, 3241 (1983).
52. Miller, D. A. B., Chemla, D. S., Damen, T. C., Gossard, A. C., Wiegmann, W., Wood, T. H., and Burrus, C. A., Phys. Rev. Lett. **53**, 2173 (1984).

53. Austin, E. J., and Jaros, M., Phys. Rev. B31, 5569 (1985).
54. Bleuse, J., Bastard, G., and Voisin, P., Phys. Rev. Lett. 60, 220 (1988).
55. Chang, Y.-C., Schulman, J. N., and Efron, U., J. Appl. Phys. 62, 4533 (1987).
56. Agullo-Rueda, F., Mendez, E. E., and Hong, J. M., Phys. Rev. B40, 1357 (1989).
57. Barrau, J., Khirouni, K., Than, D. X., Amand, T., Brousseau, M., Laruelle, F., and Etienne, B., Solid State commun. 74, 147 (1990).
58. Dignam, M. M., and Sipe, J. E., Phys. Rev. B43, 4097 (1991).
59. M. Cardona and F.H. Pollak, Phys. Rev. 142, 530(1966).
60. Yoo, J. S., and Lee, H. H., J. Appl. Phys. 71, 518 (1992).
61. Stevens, P. J., Whitehead, M., Parry, G., and Woodbridge, K., IEEE J. Quantum Electron. 24, 2007 (1988).
62. Sugg, A. R., and Leburton, J.-P. C., IEEE J. Quantum Electron. 27, 224 (1991).
63. Yuh, P. and Wang, K. L., Phys. Rev. B38, 13307 (1988).
64. Bastard, G., Brum, J. A., and Ferreira, R., "Solid State Physics," vol.44, 229-415 (1991).
65. Harwit, A., and Harris, J. S., Appl. Phys. Lett. 50, 685 (1987).
66. Wolff, D. A., Phys. Rev. 95, 1415 (1954).
67. Shockley, W., Solid-State Electron. 2, 35 (1961).
68. Baraff, G. A., Phys. Rev. 128, 2507 (1961); 133, A26 (1964).
69. Ridley, B. K., J. Phys. C16, 3373, 4433 (1983).
70. Ridley, B. K., Semicond. Sci. Technol. 2, 116 (1987).
71. Keldysh, L. V., Sov. Phys. JTEP 21, 1135 (1965).
72. Chen, Y.-Z., and Tang, T.-W., J. Appl. Phys. 65, 4279 (1989).

73. Nag, B. R., "Theory of Electrical Transport in Semiconductors," Pergamon Press (1972)
74. Seeger, K., "Semiconductor Physics: An Introduction," Solid-State Science 40, Springer-Verlag (1982).
75. Tang, J. Y., and Hess, K., *J. Appl. Phys.* 54, 5139, 5145 (1983).
76. Conwell, E. M., and Vassell, M. O., *Phys. Rev.* 166, 797 (1968).
77. Goldman, N., Wu, Y.-I., and Frey, J., *J. Appl. Phys.* 68, 1075 (1990).
78. Kane, E. O., *J. Phys. Chem. Solids* 1, 82 (1956).
79. Reggiani, L., "Hot-Electron Transport in Semiconductors," Topics in Applied Physics, Vol.58, Springer-Verlag (1985).
80. Potz, W., and Vogl, P., *Phys. Rev. B* 24, 2025 (1981).
81. Cerdeira, F., and Cardona, M., *Phys. Rev. B* 5, 1440 (1972).
82. Meyer, H. J. G., *Phys. Rev.* 112, 298 (1958).
83. Monch, W., *Phys. Status Solidi* 36, 9 (1969).
84. Anderson, C. L., and Crowell, C. R., *Phys. Rev. B* 5, 2267 (1972).
85. Chwang, R., Kao, C.-W., and Crowell, C. R., *Solid-State Electron.* 22, 599 (1979).
86. Shichijo, H., and Hess, K., *Phys. Rev. B* 23, 4197 (1981).
87. Kane, E. O., *Phys. Rev.* 159, 624 (1967).
88. Marsland, J. S., *Solid-State Electron.* 30, 125 (1987).
89. Lee, C. A., Logan, R. A., Batdorf, R. L., Kleimack, J. J., and Wiegman, W., *Phys. Rev.* 134, A176 (1964).
90. Van Overstraeten, R., and De Man, H., *Solid-State Electron.* 13, 583 (1970).
91. Woods, M. H., Johnson, W. C., and Lampert, M. A., *Solid-State Electron.* 16, 381 (1973).

92. Miller, S. L., Phys. Rev. 105, 1246 (1957).
93. Logan, R. A., and Sze, S. M., J. Phys. Soc. Jpn. 21, 434 (1966).
94. Law, H. D., and Lee, C. A., Solid-State Electron. 21, 331 (1978).
95. Bulman, G. E., Robbins, V. M., Brennan, K. F., Hess, K., and Stillman, J. R., IEEE Trans. Electron Devices Lett. EDL-4, 181 (1983).
96. Pearsall, T. P., Capasso, F., Nahory, R. E., Pollack, M. A., and Chelikowsky, J. R., Solid-State Electron. 21, 297 (1978).
97. Hess, K., Tang, J. Y., Brennan, K., Shichijo, H., and Stillman, G. E., J. Appl. Phys. 53, 3327 (1982).
98. Dresselhous, G., Kip, A. F., and Kittel, C., Phys. Rev. 98, 368 (1955).
99. Wang, K. L. and Yuh, P.-F., IEEE J. Quantum Electron. 25, 12 (1989).
100. Martinet, E., Rosencher, E., Luc, F., Bois, Ph., Costard, E., and Delaitre, S., Appl. Phys. Lett. 61, 246 (1992).

BIOGRAPHICAL SKETCH

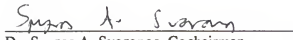
The author was born on October 28, 1961, in Seoul, Korea. He received his B.S. and M.S. in chemical engineering from Seoul National University, Korea, in 1987. After working for an additional year as a research associate in Seoul National University, he enrolled at the University of Florida for further graduate studies. His career interests are in semiconductor processing and quantum electronics.

I certify that I have read this study and that in my opinion it conforms to acceptable standards of scholarly presentation and is fully adequate, in scope and quality, as a dissertation for the degree of Doctor of Philosophy.



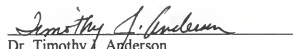
Dr. Hong H. Lee, Chairman
Professor of Chemical Engineering

I certify that I have read this study and that in my opinion it conforms to acceptable standards of scholarly presentation and is fully adequate, in scope and quality, as a dissertation for the degree of Doctor of Philosophy.



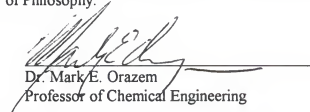
Dr. Spyros A. Svoronos, Cochairman
Associate Professor of Chemical Engineering

I certify that I have read this study and that in my opinion it conforms to acceptable standards of scholarly presentation and is fully adequate, in scope and quality, as a dissertation for the degree of Doctor of Philosophy.



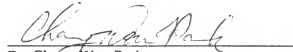
Dr. Timothy J. Anderson
Professor of Chemical Engineering

I certify that I have read this study and that in my opinion it conforms to acceptable standards of scholarly presentation and is fully adequate, in scope and quality, as a dissertation for the degree of Doctor of Philosophy.



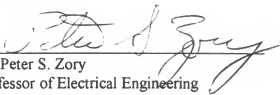
Dr. Mark E. Orazem
Professor of Chemical Engineering

I certify that I have read this study and that in my opinion it conforms to acceptable standards of scholarly presentation and is fully adequate, in scope and quality, as a dissertation for the degree of Doctor of Philosophy.



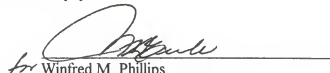
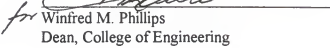
Dr. Chang Won Park
Assistant Professor of Chemical Engineering

I certify that I have read this study and that in my opinion it conforms to acceptable standards of scholarly presentation and is fully adequate, in scope and quality, as a dissertation for the degree of Doctor of Philosophy.


Dr. Peter S. Zory
Professor of Electrical Engineering

This dissertation was submitted to the Graduate Faculty of the College of Engineering and to the Graduate School and was accepted as partial fulfillment of the requirements for the degree of Doctor of Philosophy.

December 1992


for 
Winfred M. Phillips
Dean, College of Engineering

Madelyn M. Lockhart
Dean, Graduate School